

Seismic Performance of Hybrid SMA/Steel Reinforced Hollow Section Concrete Bridge Piers

Tadesse Gemedawakjira

The University of British Columbia

M. Shahria Alam (✉ shahria.alam@ubc.ca)

The University of British Columbia <https://orcid.org/0000-0002-9092-1473>

Usama Ebead

Qatar University

Research Article

Keywords: Bridge, Earthquake Engineering, Shape memory alloy, Residual drift, Self-centering, Sensitivity analysis

Posted Date: September 1st, 2021

DOI: <https://doi.org/10.21203/rs.3.rs-837858/v1>

License: © ⓘ This work is licensed under a Creative Commons Attribution 4.0 International License.

[Read Full License](#)

Seismic Performance of Hybrid SMA/Steel reinforced Hollow Section Concrete Bridge Piers

Tadesse G. Wakjira¹, M. Shahria Alam^{2*}, and Usama Ebead³

^{1,2}Applied Laboratory for Advanced Materials & Structures (ALAMS), School of Engineering, The University of British Columbia, Kelowna, BC, Canada V1V 1V7

^{1,3}Department of Civil Engineering, College of Engineering, Qatar University, P.O. Box 2713, Doha, Qatar

*Corresponding author: Tel: (250) 807-9397; *E-mail address*: shahria.alam@ubc.ca

Abstract

Concrete bridge piers reinforced with conventional steel bars experience large permanent (residual) deformation that may lead to uneconomical repair or demotion of bridges due to their non-functionality post strong seismic event. Thus, sufficiently ductile materials are required to reinforce concrete bridge piers in the plastic hinge zone in order to limit their permanent damage and deformation post-earthquake event. Previous studies showed that partial replacement of conventional steel reinforcement bars with superelastic shape memory alloy (SMA) bars in the plastic hinge zone of concrete bridge piers has the capacity to limit the residual deformation owing to the superior self-centering properties of SMA bars. In this study, the efficacy of hybrid SMA/steel reinforcement for hollow section concrete bridge piers under combined reverse cyclic and constant axial loading is numerically investigated for the first time. The responses of the piers were evaluated in terms of different performance indices including hysteretic characteristics, residual deformation, energy dissipation capacity, and self-centering capacity. A sensitivity analysis was used to explore the main effects of key design parameters and their interactions on each performance index at four damage states, namely, complete, extensive, moderate, and slight damage states. The results of this study demonstrate the effectiveness of hybrid SMA/steel reinforcement for enhancing the seismic behavior of hollow section concrete bridge piers.

Keywords: Bridge; Earthquake Engineering; Shape memory alloy; Residual drift; Self-centering; Sensitivity analysis.

1. Introduction

Residual (permanent) deformation and its amplitudes play an essential role in the seismic performance, functionality, and reparability assessment of the civil infrastructure following a strong earthquake event (Ramirez and Miranda 2012). In many major earthquakes, excessive residual displacement of piers resulted in an extensive repair or even total demolition of conventional steel reinforced concrete (RC) bridges due to their loss of functionality. For example, following the 1995 Kobe earthquake, 88 bridge columns were demolished and replaced simply because of large permanent deformation (>1.75% drift) although the damage in some of the columns was moderate and repairable, resulting in a large economic loss (Fujino et al. 2005). Another example was the 2011 Christchurch earthquake in New Zealand that caused the demolition of a large number of buildings due to unacceptable damage and residual deformation, which led to an estimated reconstruction cost of NZ\$40 billion (Wood et al. 2016).

The use of superelastic shape memory alloy (SMA) bars in the plastic hinge zone of a structural member has shown to be an effective intervention technique to control residual deformation due

47 to its favorable properties related to its capability to undergo large plastic deformation and recover
48 its original undeformed shape upon unloading (DesRoches et al. 2004; Palermo et al. 2006; Saiidi
49 and Wang 2006; Abdulridha et al. 2013; Hosseini et al. 2015, 2019; Tazarv and Saiidi 2015; Wang
50 and Zhu 2018; Zheng and Dong 2019; Hosseini and Gencturk 2019; Navarro-Gómez and Bonet
51 2019; Pereiro-Barceló et al. 2019; Xing et al. 2020). Previously, SMA was primarily applied as a
52 replacement of conventional steel longitudinal reinforcing bars in the plastic hinge zone. Saiidi
53 and Wang (Saiidi and Wang 2006) explored the potential application of SMA for reinforcing the
54 plastic hinge area of bridge piers to control residual displacement for the first time (Saiidi and
55 Wang 2006). Based on the results of the shake table, the authors reported that bridge columns
56 reinforced with superelastic Nickel-Titanium (NiTi) SMA bars exhibited considerably lower
57 residual displacement relative to conventional reinforced concrete piers. The piers reinforced with
58 SMA were capable of recovering nearly all plastic deformation after the excitation. Saiidi et al.
59 (Saiidi et al. 2009) further studied the performance of SMA reinforced bridge piers based on the
60 test results of three comparable 1/5-scaled piers under quasi-static cyclic loads. One of the columns
61 was reinforced with conventional steel bars to act as a reference. The plastic hinge area of the
62 second and third columns were reinforced with SMA bars with normal concrete in the second
63 column and engineering cementitious composite (ECC) in the third column. The SMA reinforced
64 bridge column exhibited substantially lower permanent drift, and the incorporation of ECC in the
65 plastic hinge zone reduced the damage in the column base (Saiidi et al. 2009). The reduction in
66 residual displacement for the column reinforced with SMA and conventional concrete was 67%,
67 while this reduction was increased to 83% in the column incorporating ECC and SMA (Saiidi et
68 al. 2009). Similarly, based on the experimental results of a four-span bridge model with six piers
69 under the shake table, Noguez and Saiidi (Noguez and Saiidi 2012) concluded that the use of SMA
70 and ECC significantly minimized the residual displacement and seismic damage of the piers. The
71 increased resilience of bridge columns incorporating superelastic SMA and ECC has also been
72 shown by (Hosseini et al. 2015, 2019; Hosseini and Gencturk 2019).

73 Despite its superior self-centering capacity, drawbacks particularly related to its cost limits the
74 wide application of SMA reinforcement in the full section of the plastic hinge zone (Xiang et al.
75 2020). Furthermore, the flag-shaped hysteresis properties in SMA reinforcement reduce the energy
76 dissipation capacity of the structures relative to the conventional steel reinforcement (Xiang et al.
77 2020). As a result, hybrid SMA/steel reinforcement that combines the self-centering capacity of
78 SMA reinforcement and energy dissipation capacity of conventional steel reinforcement was
79 proposed as an effective and economical reinforcement in the plastic hinge zone of solid concrete
80 bridge piers (Mao et al. 2019; Xiang et al. 2020). However, the authors believe further
81 investigation is required to enrich the literature on the hybrid SMA/steel reinforced RC bridge
82 piers. Moreover, to the best of the authors' knowledge, the literature lacks parametric investigation
83 of the significance of key design parameters and interaction effects on the seismic performance of
84 hybrid SMA/steel reinforced piers. Therefore, the current study investigates the performance of
85 hybrid SMA/steel reinforcement for reinforcing the plastic hinge zone of hollow section bridge
86 piers for the first time. An RC pier with hollow section constitutes a structurally efficient
87 construction system owing to its high strength-to-mass and stiffness-to-mass ratios and reduction
88 in the self-weight of the piers and its adverse effect compared to solid RC pier of the same cross-
89 sectional area (Kusumawardaningsih and Hadi 2010; AlAjarmeh et al. 2020).

90 The first part of this study numerically investigates the seismic performance of hybrid
91 SMA/steel reinforced hollow bridge piers. Four types of commercially available SMA bars;
92 namely, Ni₅₅Ti₄₅ (Alam et al. 2008), Ni₅₁Ti₄₉ (Ghassemieh et al. 2012), FeMnAlNi (Omori et al.

93 2011), Cu-Al-Mn (Shrestha et al. 2013) are used in the hybrid SMA/steel reinforcement. The cyclic
94 responses of the piers in terms of different performance indices such as lateral load capacity,
95 residual displacement, energy dissipation capacity, and self-centering capacity were numerically
96 investigated. In the second part, sensitivity analysis is conducted to explore the effect of various
97 key design parameters on each performance index at various damage states. Therefore, the current
98 paper has two main objectives: (a) investigating the lateral cyclic performance of hybrid SMA/steel
99 reinforced hollow section bridge piers, and (b) identifying the most significant design factors and
100 interactions on the seismic performance of such piers.

101 **2. Geometry and Model of Hollow Bridge Pier**

102 The behavior of SMA/steel reinforced RC hollow bridge piers subjected to reversed cyclic and
103 constant axial loads was investigated. For this purpose, five RC circular hollow bridge pier
104 specimens were considered in the first part of the study, one bridge pier specimen was reinforced
105 with steel bars only to act as a reference, while the other pier specimens were reinforced with
106 different types of commercially available SMA bars in addition to longitudinal steel bars.
107

108 **2.1. Geometry of hollow bridge pier**

109 The bridge piers are assumed to be located in Vancouver, BC, Canada with site soil class C (stiff
110 soil) and are seismically designed as per the Canadian Highway Bridge Design Code (CSA-S6-
111 19) (Canadian Standards Association (2019) CAN/CSA S6-19 2019) to withstand seismic ground
112 motion with a probability of 2% in 50 years corresponding to a return period of 2475 years. **Figures**
113 **1a and 1b** show the geometry of the piers. Each pier specimen has an outer diameter (D) of 1800
114 mm and a wall thickness (t) of 250 mm resulting in a wall thickness to outer diameter ratio of
115 0.139. For t/D of 0.1, a single layer of lateral reinforcement is recommended as the provision of
116 double layers of reinforcement has no significant effect on the confinement of the piers; however,
117 it may result in congestion of reinforcement bars (Liang and Sritharan 2018). Thus, a single layer
118 of reinforcement is used for all piers, as shown in **Fig. 1b**. The moment arm; i.e., the distance
119 between the top of the foundation and loading point is 9.0 m, corresponding to the aspect ratio
120 (H/d) of 5, which represents flexural dominated piers (Zhu et al. 2007). The longitudinal
121 reinforcement consists of 38-30M (diameter of 29.9 mm) steel bars resulting in the longitudinal
122 reinforcement ratio (ρ_{sl}), referred to the core concrete net area, of 2.38%, as shown in **Fig. 1b**, as
123 shown in **Fig. 1b**.

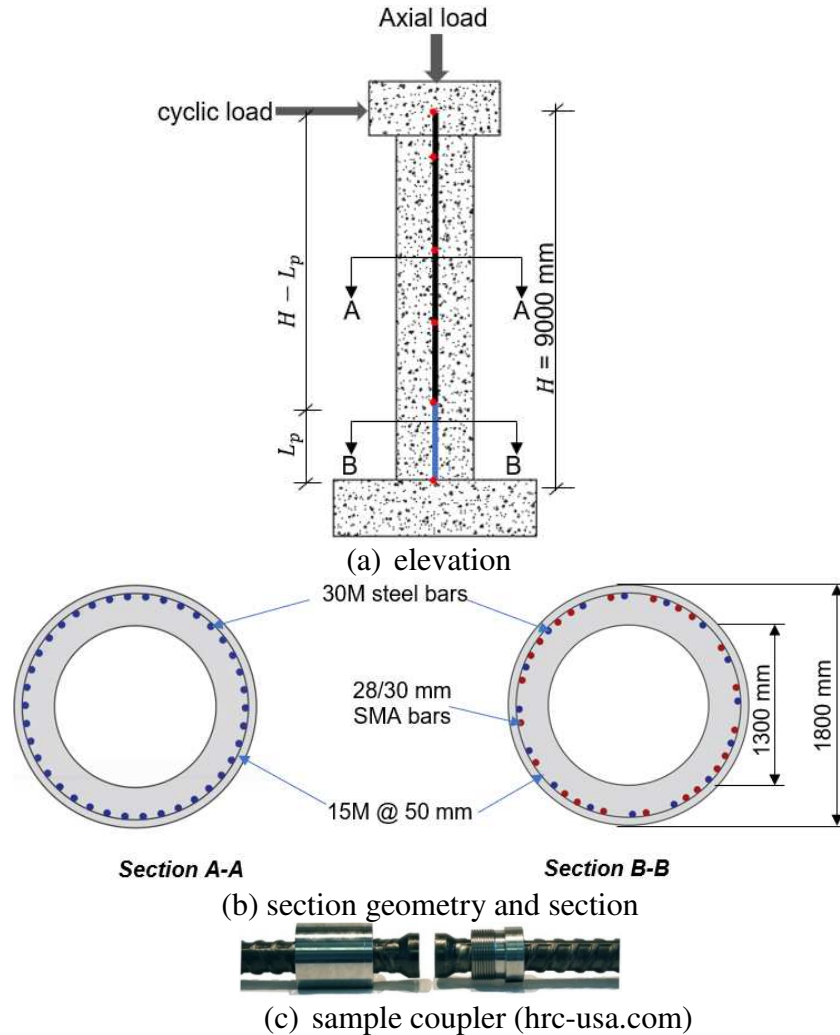


Fig. 1: Geometry and section details of hybrid SMA/steel reinforced piers.

124
125

126 The transverse reinforcement involves 15M (diameter of 16.0 mm) steel spirals with a pitch of 50
127 mm resulting in a volumetric reinforcement ratio (ρ_{st}), referred to the core concrete net volume,
128 of 1.89% (**Fig. 1b**). The steel bars used for both the longitudinal and transverse reinforcement had
129 yield strength of 475 MPa. The plastic hinge zone is reinforced with hybrid SMA/steel
130 reinforcement, in which the connection of SMA bars with steel on both sides is done with the use
131 of couplers (**Fig. 1c**) (Mostafa Tazarv M. Saiid Saiidi 2015; Tazarv and Saiidi 2016a; Dahal and
132 Tazarv 2020). Due to the unavailability of the plastic hinge length (PHL) expression for hybrid
133 SMA/steel reinforced members, the formulations for conventional RC members based on Priestley
134 et al. (Priestley et al. 1996) and CSA-S6-19 (Canadian Standards Association (2019) CAN/CSA
135 S6-19 2019) and that for SMA reinforced members proposed by Billah and Alam (Billah and
136 Shahria Alam 2016) Eqs. 1–3, respectively, were considered. The PHL is then taken as the
137 maximum of the results from the three expressions for PHL (Eqs. 1–3).

$$L_p = 0.08H + 0.022f_y d_b \leq 0.044f_y d_b \quad (1)$$

$$L_p = \max \begin{cases} D \\ H/6 \\ 450 \text{ mm} \end{cases} \quad (2)$$

$$L_p = \left[1.05 + 0.25 \frac{P}{f'_c A_g} + 0.08 \frac{H}{D} + 0.0002 f_{y,SMA} - 0.16 \rho_{sl} - 0.019 f'_c - 0.24 \rho_{st} \right] D \quad (3)$$

138 where d_b is the diameter of longitudinal bars, P is the axial load, f'_c is the compressive strength of
 139 concrete, A_g is the cross-section area of the pier, f_y is the yield strength of steel reinforcement, and
 140 ρ_{SMA} and $f_{y,SMA}$ are the reinforcement ratio and yield strength of SMA reinforcement, respectively.

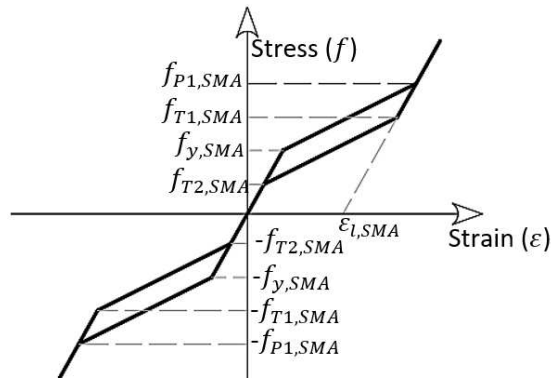
141 Four types of superelastic SMA bars are considered for the hybrid SMA/steel reinforcement. **Table**
 142 **1** presents the mechanical properties of each type of SMA, and the parameters used to define the
 143 superelastic SMA are shown in **Fig. 2** based on (Auricchio and Sacco 1997).

144
 145

Table 1: Properties of superelastic SMAs used in this study

SMA type	SMA name	E_{SMA} (MPa)	$f_{y,SMA}$ (MPa)	$f_{P1,SMA}$ (MPa)	$f_{T1,SMA}$ (MPa)	$f_{T2,SMA}$ (MPa)	$\epsilon_{l,SMA}$ (%)
Type- 1	Ni ₅₅ Ti ₄₅ (Alam et al. 2008)	62500	401	510	370	130	6.00
Type- 2	Ni ₅₁ Ti ₄₉ (Ghassemieh et al. 2012)	68000	435	535	335	170	8.00
Type- 3	FeMnAlNi (Omori et al. 2011)	98400	320	442.5	210.8	122	6.13
Type- 4	Cu-Al-Mn (Shrestha et al. 2013)	28000	210	275	200	150	9.00

146 $f_{y,SMA}$: austenite to martensite starting stress; $f_{P1,SMA}$: austenite to martensite finishing stress; $f_{T1,SMA}$: martensite to
 147 austenite starting stress, $f_{T2,SMA}$: martensite to austenite finishing stress; $\epsilon_{l,SMA}$: maximum residual strain; and $E_{a,SMA}$:
 148 modulus of elasticity



149 **Fig. 2:** One-dimensional stress-strain model for superelastic SMA (Auricchio and Sacco 1997).

150

151 The bridge piers are designed to have comparable flexural capacities, as shown in **Fig. 3**. Details
 152 of the test matrix included in the first part of the study are provided in **Table 2**. The bridge pier
 153 specimens are labeled as *S-HP-Si*: where “S” stands for specimen, “HP” stands for hollow section
 154 pier, the second “S” stands for SMA, and numeral *i* shows the type of SMA bar, as listed in **Table**
 155 **2**. Specimen S-HP-R is a reference pier reinforced with 38 $\phi 30$ mm conventional steel bars. The
 156 SMA reinforcement in the hybrid SMA/steel reinforced piers involves, 22 $\phi 28$ mm Type-1 SMA,
 157 22 $\phi 28$ mm Type-2 SMA, 30 $\phi 28$ mm Type-3, and 36 $\phi 30$ mm Type-4 SMA bars in addition
 158 to 16 $\phi 30$ mm of steel bars in the plastic hinge zone of Specimens S-HP-S1, S-HP-S2, S-HP-S3,
 159 S-HP-S4 piers, as listed in **Table 2**. All piers are reinforced with 38 $\phi 30$ mm steel rebar outside
 160 the plastic hinge zone. The piers are subjected to an axial load of 10% of the nominal axial capacity
 161 ($f'_c A_{c,net}$) and a displacement controlled cyclically increasing reverse lateral load based on
 162 ACI 374.2R-13 specifications (2013a). As shown in **Fig. 4**, the cyclic loading involved
 163 subsequently increasing drift levels with repeated cycles (2 cycles) at each drift level.

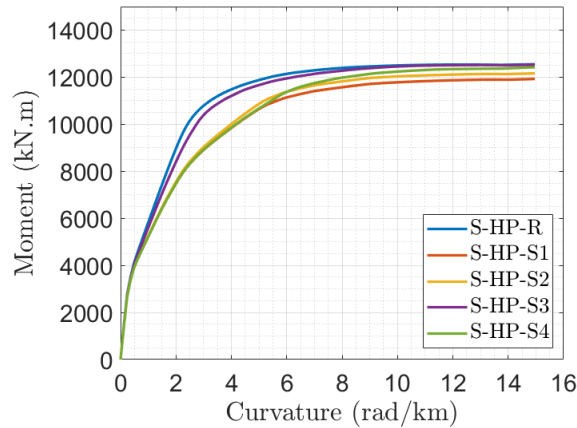
164

Table 2: Test matrix

Specimen ID	SMA type in the plastic hinge zone	
	Type	SMA reinforcement
S-HP-R	-	-
S-HP-S1	Ni ₅₅ Ti ₄₅ (Alam et al. 2008)	22 ϕ 28 mm
S-HP-S2	Ni ₅₁ Ti ₄₉ (Ghassemieh et al. 2012)	22 ϕ 28 mm
S-HP-S3	FeMnAlNi (Omori et al. 2011)	30 ϕ 28 mm
S-HP-S4	Cu-Al-Mn (Shrestha et al. 2013)	36 ϕ 30 mm

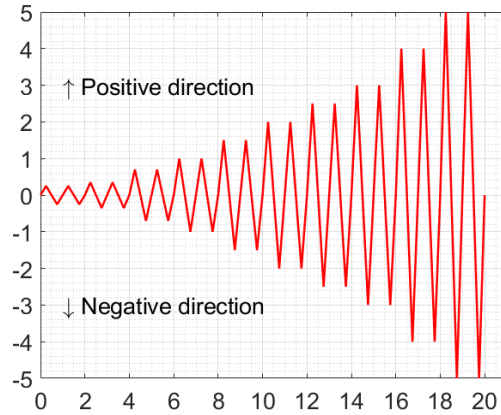
165

166



167
168

Fig. 3: Moment–curvature relationship.



169
170

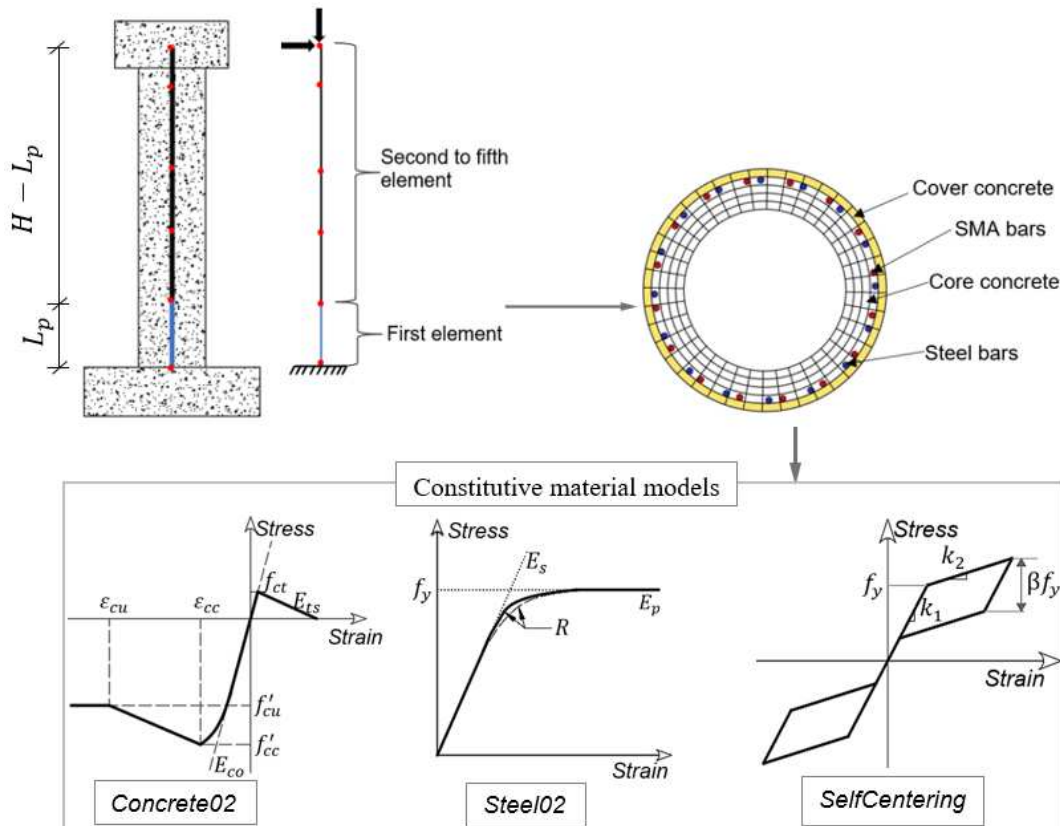
Fig. 4: Lateral reverse cyclic displacement history.

171 **2.2. Finite element modelling of the piers**

172 The numerical model of the hollow section bridge piers is created with the use of OpenSEES
 173 platform (McKenna et al. 2000). Nonlinear beam-column element (Taucer et al. 1991) with fiber
 174 section that considers both geometric nonlinearity and the spread of plasticity along the length and
 175 cross-sectional area of the element is utilized to model the piers in the present study provided its
 176 great efficiency. **Figure 5** shows a schematic view of the nonlinear fiber model and the fiber
 177 section details for the RC hollow piers. All pier specimens were longitudinally represented using
 178 five displacement-based nonlinear beam-column elements (**Fig. 5**). The cross-section of the fiber
 179 element is discretized into steel fibers and concrete fibers. The latter was further discretized as

180 core fibers (confined concrete) and cover fibers (unconfined concrete). Additional SMA fibers are
 181 included in the cross-section of the fiber element within the plastic hinge region of hybrid
 182 SMA/steel reinforced piers (**Fig. 5**).

183 The nonlinear constitutive material models are used to incorporate the material inelasticity.
 184 The longitudinal reinforcing steel bars were modelled using the nonlinear steel model of Giuffrè-
 185 Menegotto-Pinto (Menegotto and Pinto. 1973) (GMP) along with the isotropic strain hardening
 186 rules of Filippou et al. (Filippou et al. 1983), implemented into OpenSees (McKenna et al. 2000)
 187 as *Steel02* uniaxial material model. The SMA reinforcement is modelled using the uniaxial *Self-*
 188 *Centering* material model (Auricchio and Sacco 1997; Christopoulos et al. 2008).



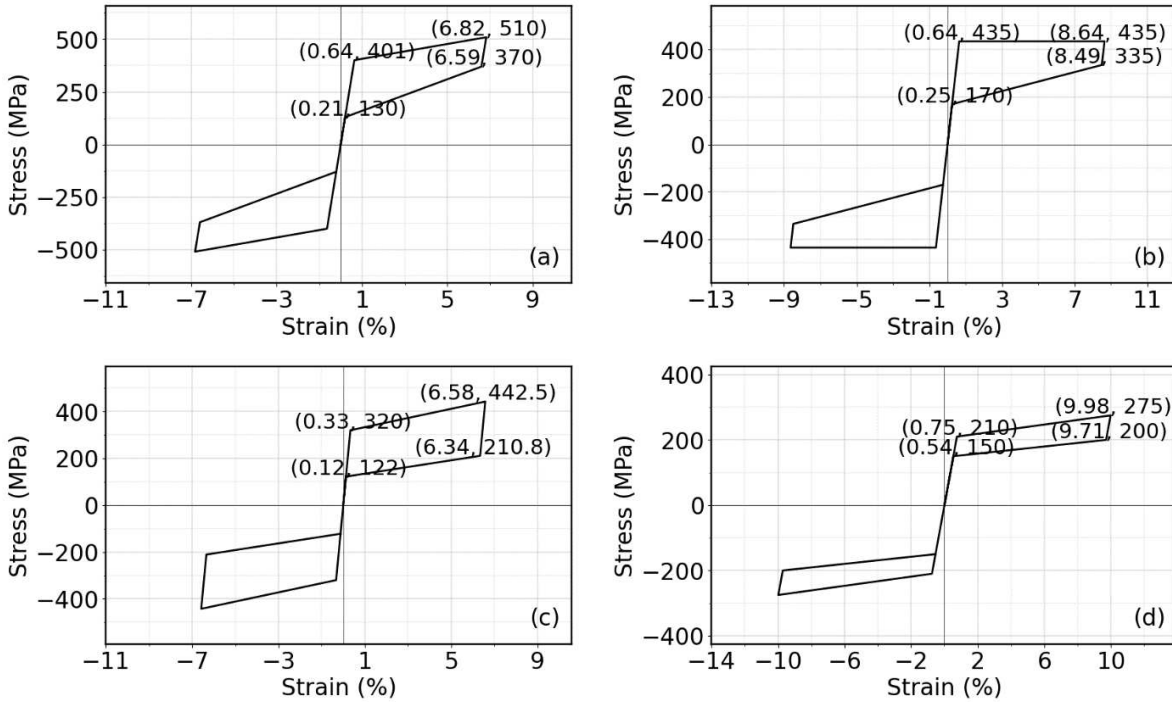
189 **Fig. 5:** The fiber-based finite element model of the novel hollow section bridge piers used in this
 190 study.

191
 192 **Figures 6a–6d** show the analytical model for the different types of SMA bars. This model has
 193 been successfully implemented to model SMA when used as reinforcement in concrete structural
 194 elements (e.g. (Alam et al. 2008; Youssef et al. 2008; Billah and Alam 2012; Nahar et al. 2019;
 195 Abraik and Youssef 2021)). It should be noted that the considered SMA material model neglects
 196 residual strain and its accumulation where its contribution to residual drift of column is negligible.
 197 Because the major damages and residual drift experienced by SMA RC elements mainly come
 198 from the damages in concrete, which has been evident from past experiments [40] and extensive
 199 numerical simulations (Alam et al. 2008; Youssef et al. 2008; Billah and Alam 2012, 2016; Nahar
 200 et al. 2019; Abraik and Youssef 2021). The behavior of concrete is modelled using the Kent and
 201 Park (Kent and Park 1971) model which followed the constitutive relationship modified by Yassin
 202 (Yassin 1994), implemented in OpenSees (McKenna et al. 2000) as *Concrete02* uniaxial material

203 model with linear tension softening. The influence of confinement of the concrete fibers due to
 204 transverse reinforcement was accounted for by modifying the concrete constitutive law of the
 205 confined concrete based on Mander et al. (Mander et al. 1989). For modelling the concrete
 206 behavior, it is required to determine the ultimate concrete strain (ϵ_{cu}) values. The ultimate concrete
 207 compressive strain of concrete in specimens confined with steel spirals only is determined based
 208 on Pauly and Priestley (Pauly and Priestley 1992) model:

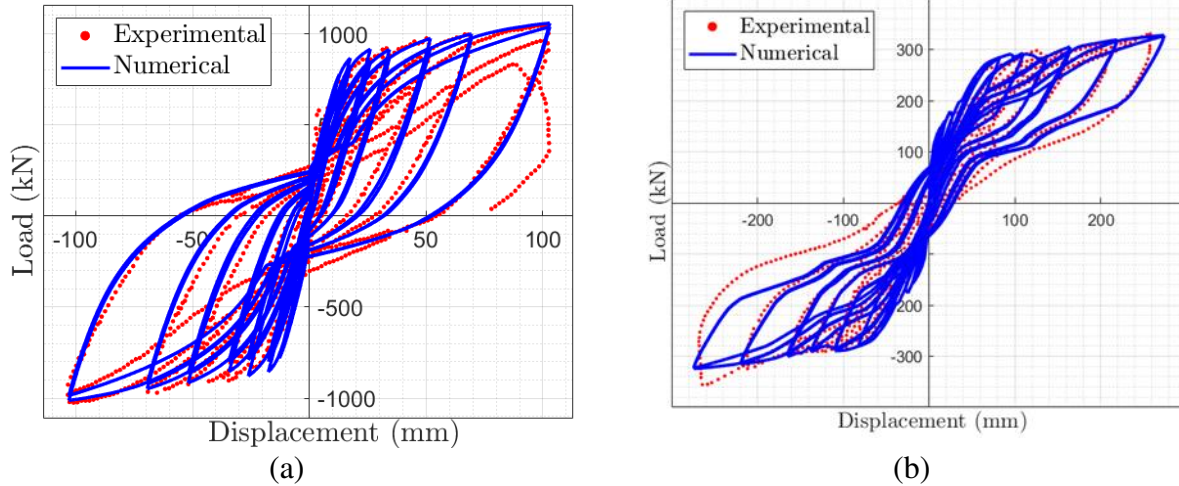
$$\epsilon_{cu} = 0.004 + 1.4\rho_{st}f_{yp}\epsilon_{sm}/f'_c \quad (4)$$

209 where f_{yp} is the yield strength of spiral bars and ϵ_{sm} is the strain in steel at maximum tensile stress.
 210



211 **Fig. 6:** Analytical models of SMA bars: (a) $Ni_{55}Ti_{45}$ (Alam et al. 2008), (b) $Ni_{51}Ti_{49}$ (Ghassemieh
 212 et al. 2012), (c) FeMnAlNi (Omori et al. 2011), and (d) Cu-Al-Mn (Shrestha et al. 2013).
 213

214 It is important to validate and calibrate the numerical model to achieve realistic results. The
 215 numerical model used in this study is validated against an experimental result of flexural deficient
 216 hollow section conventional RC bridge pier tested by Ranzo and Priestley (Ranzo and Priestley
 217 2001) (**Fig. 7a**) and SMA reinforced solid RC bridge pier (**Fig. 7b**). The numerical model predicts
 218 the load versus displacement hysteretic response of the bridge piers with acceptable accuracy
 219 (**Figs. 7a and 7b**).



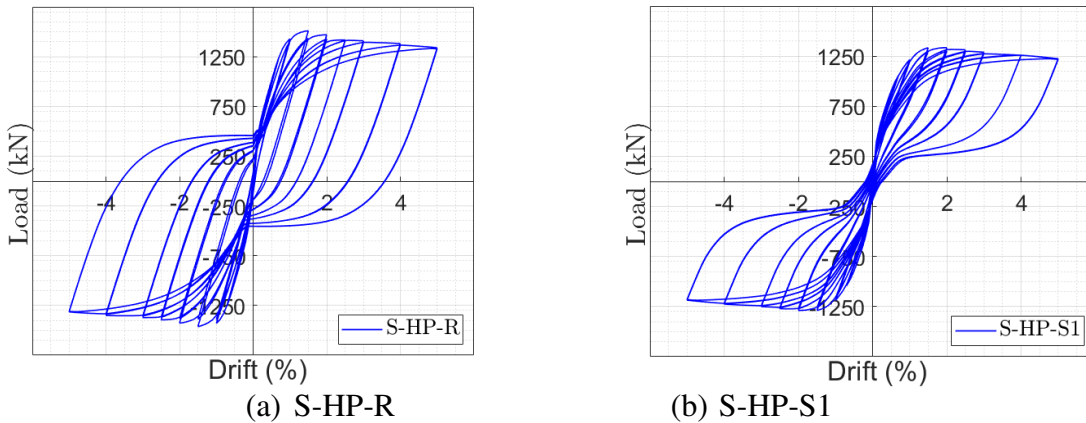
220 **Fig. 7:** Comparison of the experimental and numerical lateral load–displacement hysteretic
 221 response of (a) hollow section conventional RC bridge pier (Ranzo and Priestley 2001) and (b)
 222 SMA reinforced solid bridge pier (Tazarv and Saiidi 2016b).

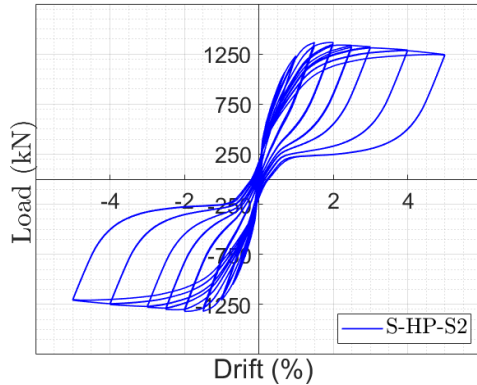
223 **3. Performance of hybrid SMA/steel reinforced piers**

224 In this section, the novel hybrid SMA/steel system is investigated as reinforcement in the plastic
 225 hinge zone of hollow section concrete bridge piers. The performance of the novel bridge piers is
 226 compared with that of the conventional RC pier of comparable flexural capacity. Different seismic
 227 performance indices were used including the lateral load versus drift response, residual
 228 (permanent) drift, energy dissipation capacity, and self-centering capacity as discussed below.

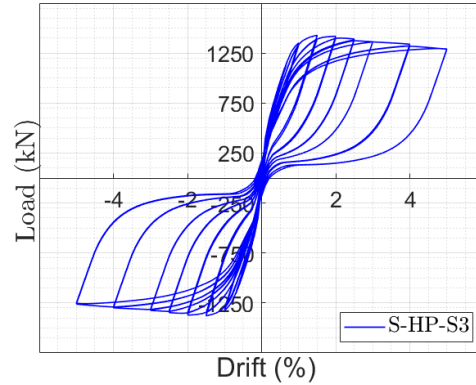
229 **3.1. Lateral load capacity and residual drift**

230 **Figures 8a–8e** show the hysteretic curves for cyclic lateral load–displacement responses, while
 231 **Fig. 9** shows the corresponding envelopes for all piers generated by joining the peak points in the
 232 first cycle of each drift level. As observed in these figures, the novel and reference bridge piers
 233 showed comparable lateral load capacity. However, the novel bridge piers showed better behavior
 234 in terms of the residual drift. The residual drift is a vital performance index for assessing the
 235 seismic performance of bridge piers and their functionality in post-seismic event. It can be
 236 determined as the mean of the residual drift ratio in the positive (push) and negative (pull)
 237 directions at the second hysteretic loop of each load level.

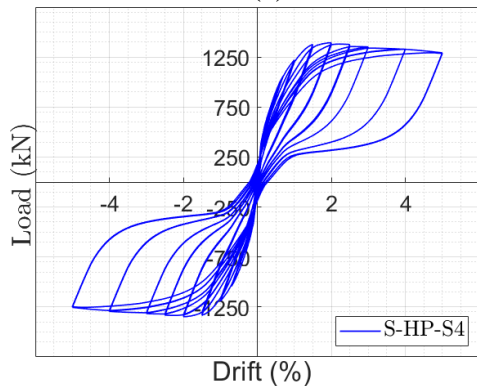




(c) S-HP-S2

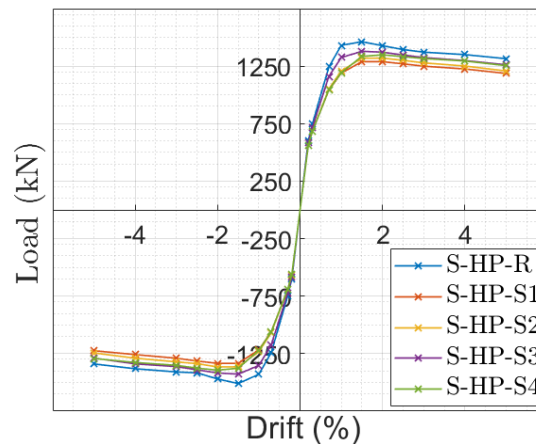


(d) S-HP-S3



(e) S-HP-S4

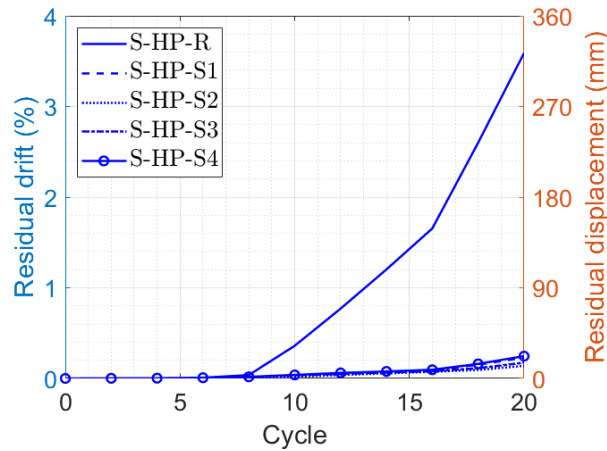
238 **Fig. 8:** Hysteretic load versus displacement response.
239



240 **Fig. 9:** The load–displacement envelope curves for the reference and hybrid SMA/steel reinforced
241 piers.

242 **Figure 10** shows the variation of residual drift ratio at increased loading cycle where the novel
243 bridge piers exhibited significantly reduced residual displacement/drift relative to the reference
244 pier. For instance, the residual drift ratio of the reference pier at cycle # 20 is 3.59%, which is
245 reduced by 93.6%, 96.1%, 95.2%, and 93.1% in Specimens S-HP-S1, S-HP-S2, S-HP-S3, and S-
246 HP-S4, respectively, relative to S-HP-R. This result shows that the hybrid SMA/steel
247 reinforcement is effective in controlling the permanent deformation of hollow bridge piers; thus,
248 enhance the seismic resilience of the piers. Generally, all SMA types showed comparable residual

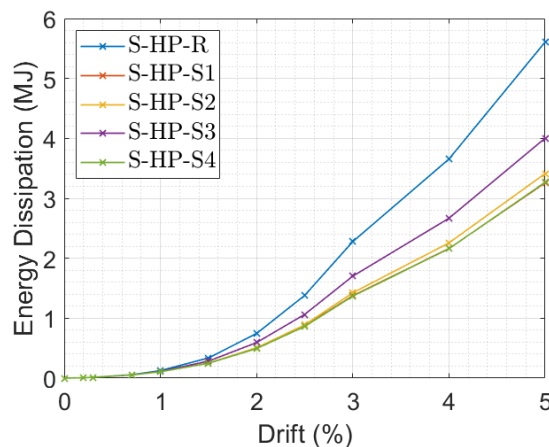
249 drift at all drift levels in Specimens S-HP-S1, S-HP-S2, S-HP-S3, and S-HP-S4, as shown in **Fig.**
 250 **10**.



251 **Fig. 10:** Residual drift ratio and displacement versus loading cycle.
 252

253 3.2. Energy dissipation and self-centering capacities

254 The hysteretic energy dissipation (E_a) of the piers can be determined as the area under the lateral
 255 load versus displacement curves at each loading cycle, as specified in ASCE 41-13 (2013b). The
 256 cumulative E_a is computed for each specimen as a sum of the energy dissipated in consecutive
 257 cycles and plotted versus the corresponding drift ratio in **Fig. 11** for all specimens. As shown in
 258 this figure, the hybrid SMA/steel reinforced piers exhibited lower E_a compared to the reference
 259 pier as the hysteretic curves in the novel piers are controlled by the flag-shaped behavior of
 260 superelastic SMA bars. For the novel piers, Specimen S-HP-S3 reinforced with FeMnAlNi SMA
 261 dissipated the highest energy (**Fig. 11**).



262 **Fig. 11:** Cumulative energy dissipation capacity at each drift level.
 263

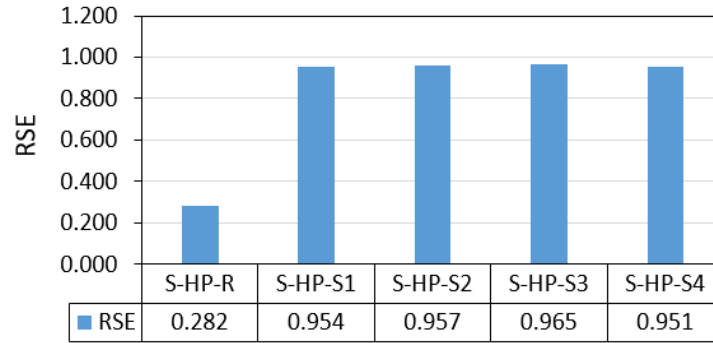
264 The efficacy of the novel hybrid SMA/steel reinforcement in improving the seismic
 265 performance of the piers can be demonstrated by the self-centering capacity of the piers, which
 266 can be quantified in terms of the relative self-centering efficiency (RSE) (Sideris et al. 2014):

$$RSE = 1 - \frac{u_{res}^+ - u_{res}^-}{u_{peak}^+ - u_{peak}^-} \quad (5)$$

267 where u_{res}^+ and u_{res}^- are the residual displacements in the positive (push) and negative (pull)
 268 directions, respectively, while u_{peak}^+ and u_{peak}^- are the positive peak displacement and the negative
 269 peak displacement, respectively.

270 **Figure 12** compares the self-centering efficiency of the piers during the last loading cycle, the
 271 piers reinforced with hybrid SMA/steel reinforcement exhibited significantly higher self-centering
 272 capacity compared to the reference pier reinforced with conventional steel reinforcement owing to
 273 the excellent self-centering capacity of superelastic SMA bars. The *RSE* of Specimen S-HP-R
 274 during the last loading cycle was 0.282, as can be seen in **Fig. 12**. The use of hybrid SMA/steel
 275 reinforcement in the novel piers significantly improved the self-centering capacity of the piers.
 276 The *RSE* for the novel piers at the last loading cycle ranged between 0.951–0.965 which represents
 277 a 237–242% increase in *RSE* relative to that for S-HP-R, as shown in **Fig. 12**.

278



279 **Fig. 12:** Self-centering capacity of the piers.

280

281 It is crucial to identify the important factors and interactions between the factors to fully understand
 282 the seismic behavior of hybrid SMA/steel reinforced hollow bridge piers. Thus, in the following
 283 section, a sensitivity analysis is conducted to explore the significance of the effect of various
 284 parameters on the performance of the novel hollow bridge piers.

285 4. Sensitivity Analysis

286 In this section, a commonly used superelastic SMA bars, NiTi-SMA (Type-1 in **Table 1**), is used
 287 to explore the important parameters and interactions on the performance of the novel hollow bridge
 288 piers reinforced with hybrid SMA/steel reinforcement in the plastic hinge zone. Considering the
 289 uncertainty of material and geometry of the hybrid SMA/steel reinforced hollow piers, seven
 290 potential influencing factors are considered for the sensitivity study. The main factors considered
 291 for the sensitivity analysis include the yield strength of reinforcement steel bars (f_y), compressive
 292 strength of concrete (f_c'), longitudinal steel (ρ_{sl}) and SMA (ρ_{SMA}) reinforcement ratios in the
 293 plastic hinge zone, volumetric ratio of transverse reinforcement (ρ_{st}), aspect ratio (H/d), and axial
 294 load level (P/P_0). A two-level (2^k) factorial DOE was generated with the subscript k being the
 295 number of parameters (Montgomery 2013), and a reverse cyclic pushover analysis was carried out
 296 for each combination of the seven main parameters (a total of 128 hollow pier specimens).
 297 Factorial designs are commonly utilized to study the significance of different parameters
 298 influencing the response variable in multi-variable studies (Montgomery 2013). In this study, the
 299 significance of the main effect and interaction effects on the performance of the piers is assessed

300 using factorial DOE combined with the analysis of variance (ANOVA) (Montgomery 2013) at a
 301 two-sided confidence level of 95%, a significance level of 5%.

302 **Table 3** summarizes the main factors along with the levels applied for each factor based on a
 303 literature survey and design codes (Zhu et al. 2007; ACI Committee 318 2011; Wang et al. 2014).
 304 The compressive strength of concrete varied between 27 MP and 48 MPa (Reza et al. 2014; Wang
 305 et al. 2014). The yield strength of steel bars is in a range of 420 MPa to 550 MPa (ACI Committee
 306 318 2011; Wang et al. 2014). The low and high levels for the aspect ratio are considered as 4 and
 307 7, respectively, such that the piers are dominated by flexural failure (Zhu et al. 2007; Parghi and
 308 Alam 2017). The longitudinal steel and SMA reinforcement ratio in the hybrid NSM-SMA/steel
 309 reinforcement of the plastic hinge region varied from 0.7% - 1.5% and 1.0% - 2.5%, respectively.
 310 Outside the plastic hinge zone, the specimens are consistently reinforced with longitudinal steel
 311 bars of 3.5% reinforcement ratio. The ρ_{st} value ranged between 0.7% and 1.3%. The low and high
 312 levels for the axial load ratio are considered as 3% and 20%, respectively (Wang et al. 2014).
 313

314 **Table 3:** Factors and their levels used in factorial design for Hybrid NSM/SMA reinforced piers

S.N.	Main factors		Lower level (-)	Upper level (+)
1	Concrete compressive strength, f'_c (MPa)	A	27	48
2	Yield strength of steel, f_y (MPa)	B	420	550
3	Reinforcement ratio of longitudinal steel bars, ρ_{st} (%)	C	0.70	1.50
4	Volumetric ratio of transverse reinforcement, ρ_{st} (%)	D	0.70	1.30
5	Aspect ratio, H/d	E	4	7
6	Longitudinal SMA reinforcement ratio, ρ_{SMA} (%)	F	1	2.5
7	Axial load ratio, P/P_0 (%)	G	3	20

315

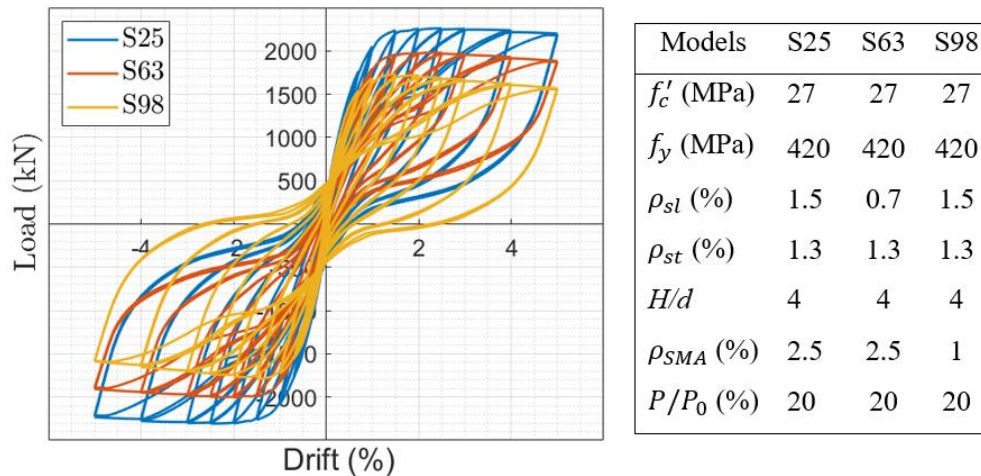
316 **4.1. Damage limit states**

317 In this study, displacement demand is used to identify the seismic damage of the hybrid SMA/steel
 318 reinforced hollow bridge piers. Four limit states defined in HAZUS-MH (FEMA 2003); namely,
 319 slight, moderate, extensive, and complete damages are adopted to describe the seismic damage of
 320 the piers. Different damage indices have been proposed in the literature to define the first
 321 occurrence of each damage state. In the first approach, the damage states are defined in terms of
 322 the strain limits in the concrete and steel reinforcement. Different empirical equations have been
 323 proposed to determine these strains at different damage states for conventional RC bridge piers,
 324 which are derived from the experimental results of conventional RC bridge piers (Berry and
 325 Eberhard 2005, 2007; Feng et al. 2015; Goodnight et al. 2016). However, no damage index has
 326 been proposed for the bridge piers reinforced with SMA and/or hybrid SMA/steel reinforcement.
 327 The second approach uses the maximum drift ratio to define the limit states. In this study, the
 328 second approach is used as the damage index corresponding to the displacement drift of 0.7%,
 329 1.5%, 2.5%, and 5% for the slight, moderate, extensive, and complete damage states of hybrid
 330 SMA/steel reinforced bridge piers, respectively. A similar approach has been used in the previous
 331 studies (e.g. (Kim and Shinozuka 2004; Yi et al. 2007; Akbari 2012; Sideris et al. 2014)). In this
 332 paper, the abbreviations DS1, DS2, DS3, and DS4 refer to the slight, moderate, extensive, and
 333 complete damage states, respectively.

334 Five seismic performance indices; namely, lateral load capacity, initial stiffness, energy
 335 dissipation capacity, residual drift, and self-centering capacity are used to investigate the
 336 performance of the piers. The lateral load–displacement responses were generated for each

337 combination of the seven factors to quantify the cyclic response of the hybrid SMA/steel reinforced
 338 hollow bridge piers (a total of 128 specimens). For instance, **Fig. 13** shows the lateral load–drift
 339 responses for Specimens S25, S63, and S98 that differ in the ρ_{SMA} and ρ_{sl} . As shown in this figure,
 340 Specimen S63 exhibited the highest self-centering capacity. The residual/permanent drift of the
 341 hybrid SMA/steel reinforced pier is observed to be significantly influenced by both SMA and steel
 342 reinforcement ratios (**Fig. 13**). The residual drift is reduced with an increase in the ρ_{SMA} , while it
 343 increased with an increase in the longitudinal steel reinforcement ratio (**Fig. 13**). In Specimen S63,
 344 the SMA reinforcement ratio is set to its upper level while ρ_{sl} is set to its low level. Consequently,
 345 Specimen S63 exhibited lower residual drift and better self-centering capacity, as can be observed
 346 in **Fig. 13**. Specimen S98, which is reinforced with a higher longitudinal steel reinforcement ratio
 347 exhibited increased residual drift compared to Specimen S63, as shown in **Fig. 13**.

348



349 **Fig. 13:** Hysteretic load versus displacement response.

350

351 4.2. Effect of key design parameters

352 As discussed earlier, the main effects and interaction effects of different factors on the response
 353 parameters are assessed using ANOVA analysis, which allows identifying the most significant
 354 factors (Montgomery 2013). A two-sided confidence interval at 95% confidence level is
 355 considered in the ANOVA analysis. Consequently, the conclusions are made comparing P -value
 356 (the smallest significance level corresponding to the significance of the data) with the significant
 357 level (5% in this study) (Montgomery 2013). Thus, the main and interaction effects with a P -value
 358 of less than 0.05 are significant at 95% confidence. The normal probability plot of standardized
 359 effect is used to determine the degree and direction of the significant effects. In this plot, the
 360 insignificant effects on the response variable fall on a fitted straight line, while the significant
 361 effects fall away from the fitted line at some distance. The distance of the factor from the fitted
 362 line signifies the degree of importance of its effect. The larger the distance between the factor and
 363 the fitted line, the higher its effect on the response variable. Besides, the normal probability plot
 364 shows the direction of the significant effects, in which the response variable increases with the
 365 positive effect, while it decreases with the negative effect. In this plot, the positive and negative
 366 significant effects fall on the right side and left side of the fitted line, respectively.

367 4.2.1. Lateral load capacity

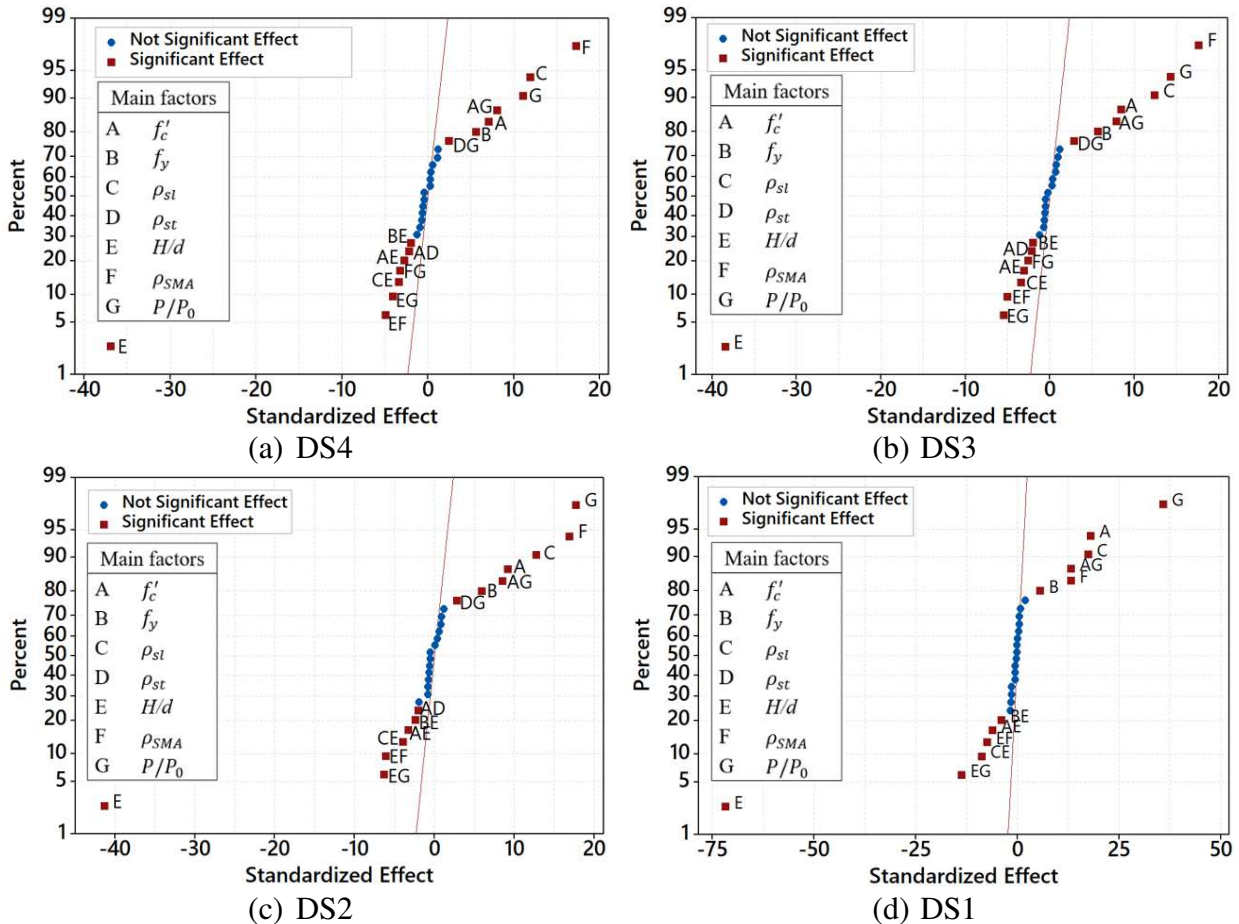
368 The ANOVA results for the lateral load capacity (P_{max}) is presented in **Table 4**.

369 **Table 4:** ANOVA results for the lateral load capacity

Damage states	DS4	DS3	DS2	DS1
Main Parameters				
A f'_c	< 0.0001	< 0.0001	< 0.0001	< 0.0001
B f_y	< 0.0001	< 0.0001	< 0.0001	< 0.0001
C ρ_{sl}	< 0.0001	< 0.0001	< 0.0001	< 0.0001
D ρ_{st}	0.2942	0.3639	0.4242	0.7321
E H/d	< 0.0001	< 0.0001	< 0.0001	< 0.0001
F ρ_{SMA}	< 0.0001	< 0.0001	< 0.0001	< 0.0001
G P/P_0	< 0.0001	< 0.0001	< 0.0001	< 0.0001
Two-way interactions				
AB	0.8068	0.7753	0.7435	0.5161
AC	0.5299	0.51	0.5065	0.761
AD	0.0293	0.0292	0.0437	0.1327
AE	0.0073	0.0024	0.0012	< 0.0001
AF	0.1901	0.2058	0.3671	0.4811
AG	< 0.0001	< 0.0001	< 0.0001	< 0.0001
BC	0.2384	0.2471	0.258	0.8463
BD	0.4438	0.4415	0.4127	0.464
BE	0.0497	0.0409	0.0163	< 0.0001
BF	0.7392	0.8201	0.9823	0.5288
BG	0.3417	0.4666	0.3954	0.1258
CD	0.6531	0.562	0.548	0.8097
CE	0.001	0.0008	0.0001	< 0.0001
CF	0.6463	0.757	0.4816	0.0961
CG	0.7955	0.5019	0.4457	0.7154
DE	0.5212	0.5536	0.5736	0.9674
DF	0.5933	0.5434	0.596	0.7731
DG	0.0182	0.0063	0.0062	0.086
EF	< 0.0001	< 0.0001	< 0.0001	< 0.0001
EG	< 0.0001	< 0.0001	< 0.0001	< 0.0001
FG	0.0016	0.0108	0.0518	0.061

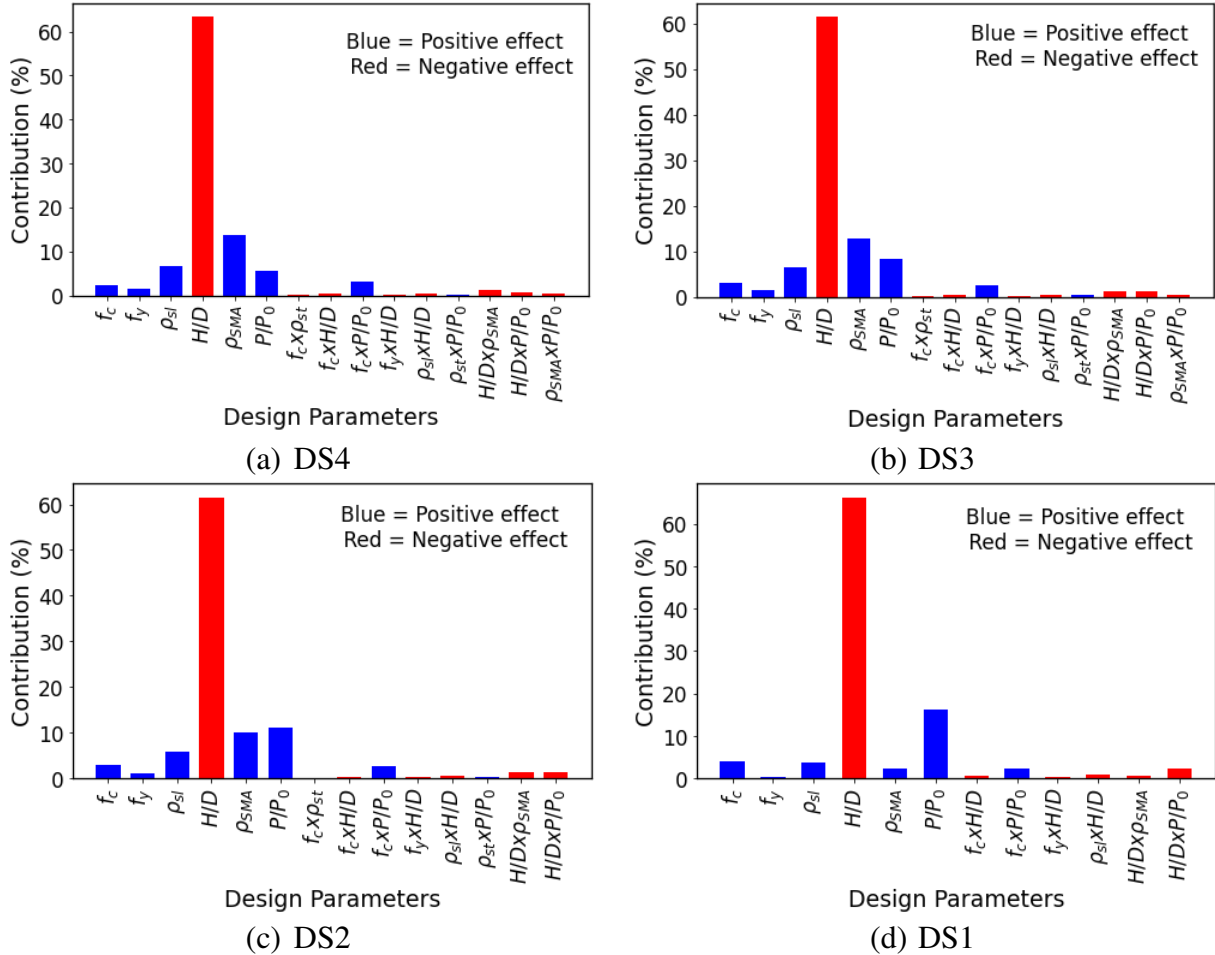
370
371 The results demonstrate that the P -values for the main effects of f'_c , f_y , ρ_{sl} , H/d , ρ_{SMA} , and P/P_0
372 at DS4 are less than 0.05. Consequently, the main effects of these parameters on P_{max} are
373 significant at the complete damage state. The transverse reinforcement showed an insignificant
374 effect on the P_{max} at damage state DS4, as listed in **Table 4**. The normal probability plot of lateral
375 load capacity in **Fig. 14a** shows the standardized main and interaction influences of the factors
376 relative to a distribution fit line at DS4. As can be observed in **Fig. 14a**, the aspect ratio showed a

377 negative significant influence on P_{max} at DS4. Thus, the load capacity decreases with an increase
 378 in the aspect ratio, as expected. Similarly, the interaction of H/d with f'_c , f_y , ρ_{sl} , ρ_{SMA} , and P/P_0
 379 showed negative significant effects on the load capacity at damage state DS4 (**Fig. 14a**). The main
 380 effects of f'_c , f_y , ρ_{sl} , ρ_{SMA} , and P/P_0 are positive; thus, the load capacity increases with an increase
 381 in these factors, as shown in **Fig. 14a**. Similarly, the interaction of P/P_0 with f'_c and ρ_{st} showed
 382 positive significant effects.
 383

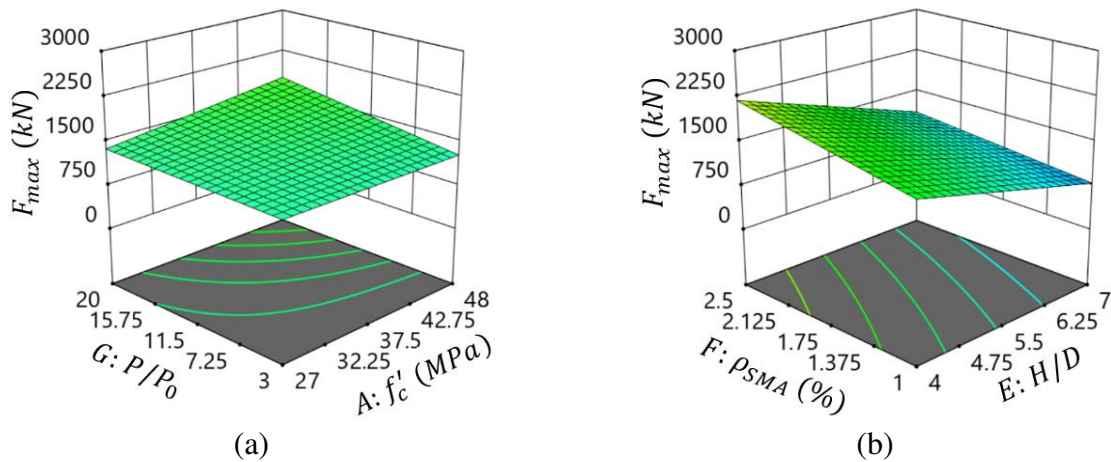


384 **Fig. 14:** Normal plot of the standardized effects for load capacity.
 385

386 **Figure 15a** demonstrates the percentage contributions of the main factors and their interactions
 387 on the load capacity at damage state DS4. The color of the bar shows the direction of the effect
 388 (blue: positive effect, red: negative effect), while the height of the bar shows the percentage
 389 contribution of the factor. As can be observed in this figure, aspect ratio showed the highest effect
 390 (63.3% contribution) on P_{max} . The SMA reinforcement in the plastic hinge zone showed the
 391 highest positive significant influence on P_{max} (**Fig. 14a** and **Fig. 15a**). The contribution of f'_c and
 392 f_y were 2.31% and 1.44%, while the contributions of all the interaction effects apart from $f'_c \times P/P_0$
 393 and $\rho_{SMA} \times H/d$ interactions were insignificant (less than 1%), as shown in **Fig. 15a**. The 3D plots in
 394 **Figs. 16a** and **16b** show the effects of the $f'_c \times P/P_0$ and $\rho_{SMA} \times H/d$ interactions on the load
 395 capacity by simultaneously varying the two factors in each figure from the lowest to upper values
 396 while keeping the other factors at their average values.



397 **Fig. 15:** Percentage contribution of the significant effects on the load capacity.



398 **Fig. 16:** Variation of load capacity with (a) P/P_0 and f'_c and (b) ρ_{SMA} and H/D .

399

400

401

402

403

At DS1, DS2, and DS3 damage states, the main effects of f'_c , f_y , ρ_l , H/d , ρ_{SMA} , and P/P_0 are shown to be significant, as listed in **Table 4** and **Figs. 14b–14d**. The aspect ratio showed the highest negative significant effect, as shown in **Figs. 14b–14d**. For the extensive damage, the SMA reinforcement ratio showed the highest positive significant effect (**Fig. 14b**) as observed for DS4,

404 while for the moderate and slight damage states the main effect of ρ_{SMA} is lower than that of axial
 405 load ratio, as shown in **Figs. 14c** and **14d**. This can also be observed in **Figs. 15b–15d** that show
 406 the contributions of the main effects and interaction effects on P_{max} at DS3, DS2, and DS1,
 407 respectively. The contribution of H/D to the load capacity varied between 61.4–66.1%, as shown
 408 in **Figs. 15b–15d**. The significance of SMA reinforcement increased with the damage states. At
 409 the slight damage state, the contribution of ρ_{SMA} was only 2.2%. This value increased to 10.2%
 410 and 12.8% at DS2 and DS3, respectively. The SMA reinforcement ratio showed the highest
 411 positive effect at DS4 and DS3, while P/P_0 showed the highest contribution for the remaining two
 412 damage states (**Figs. 15a–15d**). **Figures 15a–15d** also suggest that the effect of longitudinal
 413 reinforcement (f_y and ρ_l) increases with the damage states. For instance, the contribution of f_y to
 414 the load capacity was less than 5% at DS1, which increased to 5.77%, 6.34%, and 6.58% at DS2,
 415 DS3, and DS4, respectively. The compressive strength of concrete produced the most prominent
 416 effect at the slight damage state, DS1 compared to its effect at DS2, DS3, and DS4, as can be
 417 observed in **Figs. 15a–15d**. Prior to cracking, concrete contributes to the load capacity of the piers;
 418 however, its contribution decreases with an increase in the applied load, while the steel and SMA
 419 reinforcement resist most of the applied loads.

420 Regarding the interaction effects, similar to DS4, $f_y \times H/d$, $f'_c \times \rho_{tr}$, $f'_c \times H/d$, $\rho_{SMA} \times P/P_0$,
 421 $\rho_l \times H/d$, $H/d \times P/P_0$, and $H/d \times \rho_{SMA}$ interactions showed negative influence in their order of
 422 significance at DS2 and DS3, as shown in **Figs. 14b** and **14c** and **15b** and **15c**. The interaction of
 423 axial load ratio with f'_c and ρ_{st} showed a positive significant effect on P_{max} (**Figs. 14b** and **14c**).
 424 At DS1, the interaction of the aspect ratio with all main factors except ρ_{st} showed negative
 425 significant effect, while the $f'_c \times P/P_0$ interaction showed positive significant influence on the load
 426 capacity, as can be observed in **Fig. 14d**. The transverse reinforcement showed an insignificant
 427 effect on P_{max} at all limit states for flexural dominated bridge piers considered in this study.
 428 Similar observations have been reported for conventional RC bridge piers (e.g. (Parghi and Alam
 429 2016)).

430 **4.2.2. Initial stiffness**

431 The initial stiffness is taken as the effective stiffness corresponding to DS1 (Sideris et al. 2014). It
 432 can be determined as the slope of the line connecting the negative and positive peaks in the
 433 negative (pull) and positive (push) directions, respectively, at DS1 as given in Eq. (6).

$$434 \quad K = \frac{F_p^+ - F_p^-}{u_p^+ - u_p^-} \quad (6)$$

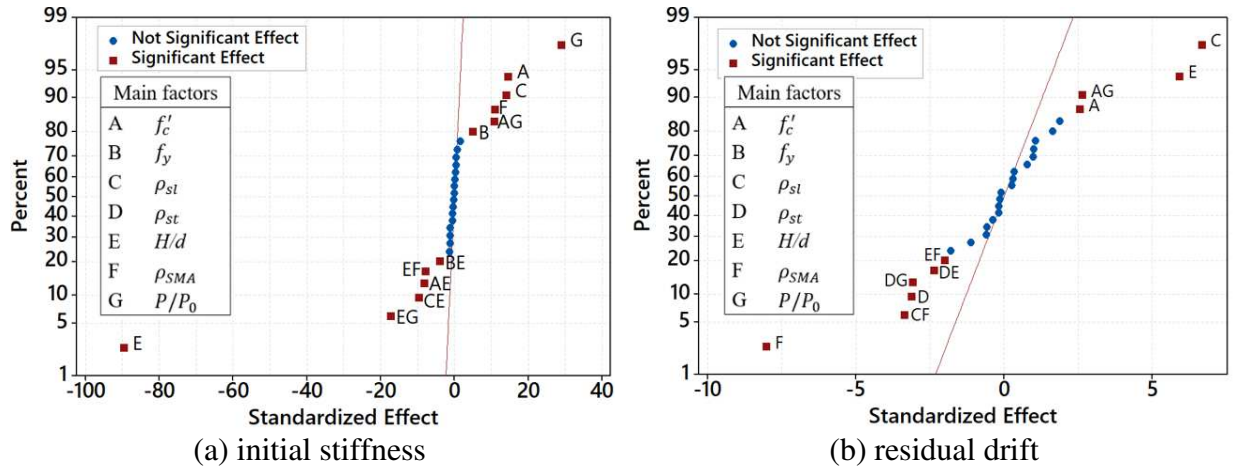
435 where F_p^- and F_p^+ are the peak load in the negative and positive directions, respectively, and u_p^-
 436 and u_p^+ are the displacements corresponding to F_p^- and F_p^+ , respectively.

437 According to the results of ANOVA analysis in **Table 5**, all factors apart from the volumetric
 438 ratio of transverse reinforcement produce significant main effects on the initial stiffness. **Figure**
 439 **17a** shows the normal plot of the standardized effects of the key design parameters on the initial
 440 stiffness at 95% confidence. The aspect ratio has a negative significant effect on the initial
 441 stiffness; thus, an increase in H/D ratio decreases the initial stiffness, as shown in **Fig. 17a**. In
 442 contrast, all other significant main effects showed positive effects on the initial stiffness.
 443 Therefore, the initial stiffness increases with an increase in f'_c , f_y , ρ_{sl} , ρ_{SMA} , and P/P_0 , as shown
 444 in **Fig. 17a**. Similarly, the $f'_c \times P/P_0$ interaction showed positive significant influence, whereas the
 445 interactions of aspect ratio with f'_c , f_y , ρ_{sl} , ρ_{SMA} , and P/P_0 reduce the initial stiffness, as observed
 446 in **Fig. 17a**.

447 **Table 5:** ANOVA results for the initial stiffness, residual drift, and *RSE*.

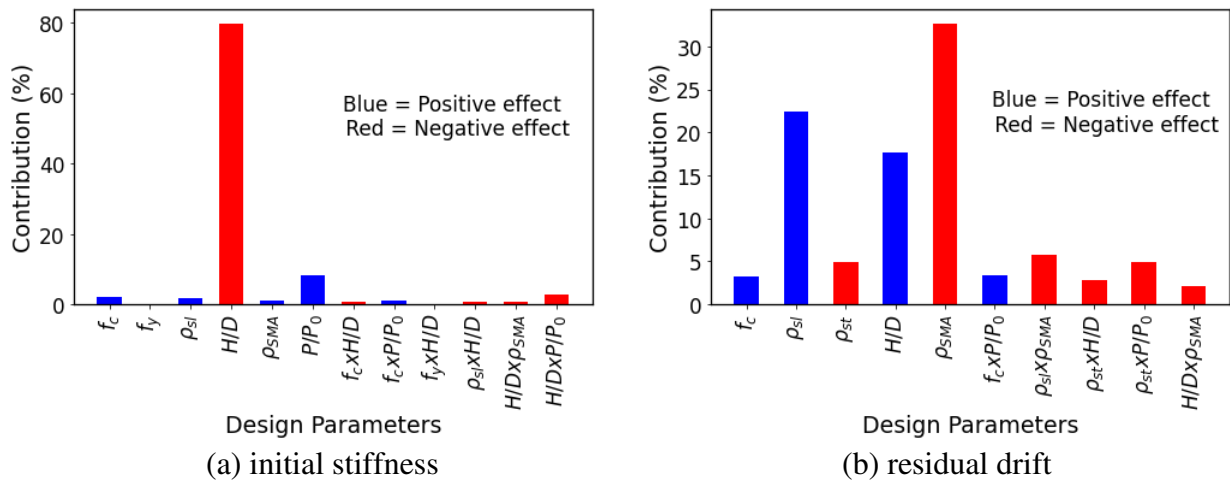
Response	Initial stiffness	Residual drift	<i>RSE</i>
Main Parameters			
A f'_c	< 0.0001	0.0128	0.0265
B f_y	< 0.0001	0.8149	0.3719
C ρ_{st}	< 0.0001	< 0.0001	< 0.0001
D ρ_{st}	0.7849	0.0022	< 0.0001
E H/d	< 0.0001	< 0.0001	0.1108
F ρ_{SMA}	< 0.0001	< 0.0001	< 0.0001
G P/P_0	< 0.0001	0.4515	0.2679
Two-way interactions			
AB	0.542	0.8725	0.534
AC	0.8012	0.3352	0.7889
AD	0.2121	0.2572	0.2926
AE	< 0.0001	0.2962	0.8571
AF	0.5616	0.8366	0.8534
AG	< 0.0001	0.0104	0.0633
BC	0.8887	0.5417	0.8402
BD	0.5432	0.7793	0.5716
BE	< 0.0001	0.8386	0.2953
BF	0.6634	0.557	0.4221
BG	0.2136	0.8991	0.7236
CD	0.9685	0.1073	0.0136
CE	< 0.0001	0.3275	0.2787
CF	0.2107	0.001	0.0002
CG	0.9331	0.0707	0.0047
DE	0.9054	0.0192	0.0821
DF	0.7507	0.0655	0.0136
DG	0.161	0.0025	< 0.0001
EF	< 0.0001	0.0461	0.9513
EG	< 0.0001	0.7461	0.986
FG	0.1652	0.6911	0.552

448



449 **Fig. 17:** Normal plot of the standardized effects.

450
 451 The axial load ratio and yield strength of longitudinal reinforcement showed the highest and
 452 lowest positive significant influences, respectively, as shown in **Fig. 17a**. This observation can be
 453 clearly observed in **Fig. 18a** that shows the percentage contributions of the significant main effects
 454 and interaction effects on the initial stiffness. As can be seen in **Fig. 18a**, aspect ratio showed the
 455 most significant influence on the initial stiffness with a percentage contribution of 79.74%. The
 456 axial load ratio is the second most significant factor, as shown in **Fig. 18a**. The contributions of
 457 SMA reinforcement, compressive strength of concrete, longitudinal steel reinforcement (f_y and
 458 ρ_l) were less than 5% (**Fig. 18a**). The contributions of the interactions of axial load ratio with f'_c
 459 and H/D were 1.14% and 2.98%, whereas other significant interactions produce less than 1%
 460 contributions each, as observed in **Fig. 18a**.



462 **Fig. 18:** Percentage contribution of the significant effects.

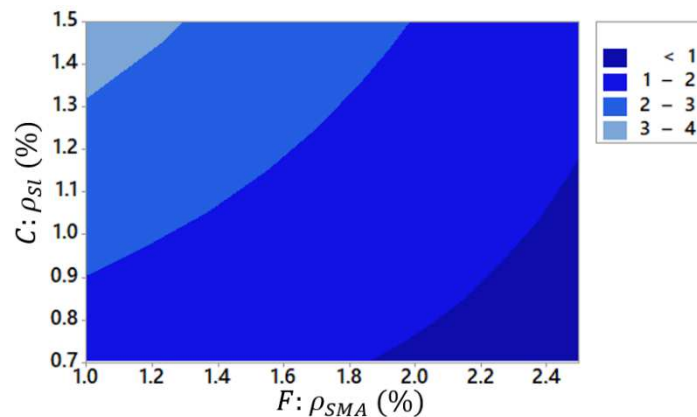
463
 464 **4.2.3. Residual drift**

465 The residual drift corresponds to the drift when the lateral load becomes zero at a complete damage
 466 state. All main factors with the exceptions of f_y and axial load ratio exhibited significant effect on
 467 the residual drift, as listed in **Table 5**. The main effects of the SMA reinforcement ratio and ρ_{st}
 468 were negative; thus, the residual drift significantly decreases with an increase in ρ_{SMA} and ρ_{st} , as

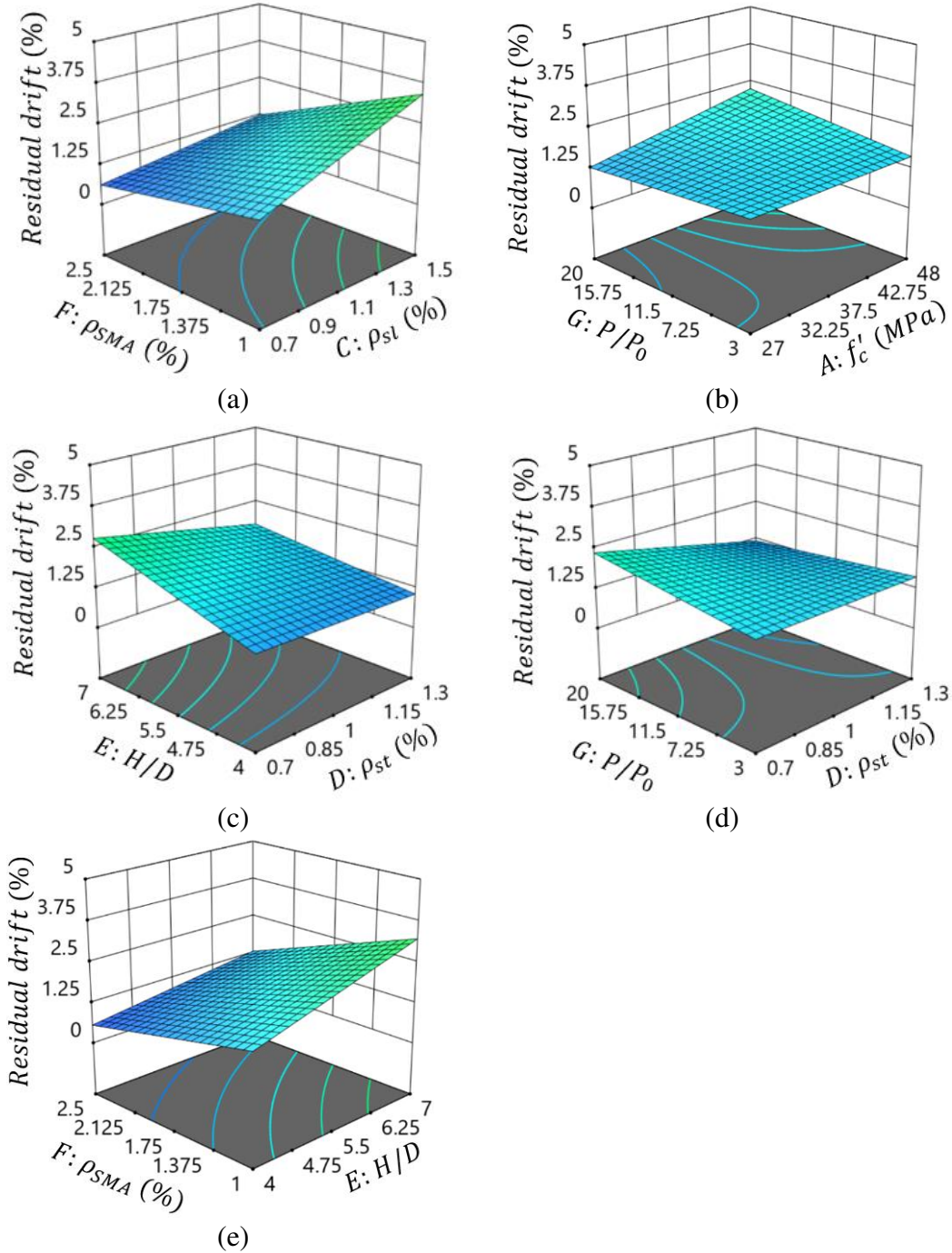
469 observed in **Fig. 17b**. Consequently, the residual drift increases with an increase in f'_c , ρ_{sl} , and
 470 aspect ratio, as shown in **Fig. 17b**. Similarly, the interaction between f'_c and axial load ratio
 471 significantly increases the residual drift, while the $\rho_{SMA} \times H/D$, $\rho_{st} \times H/D$, $\rho_{st} \times P/P_0$, $\rho_{SMA} \times \rho_{sl}$
 472 interactions showed negative significant effects on the residual drift in their order of importance,
 473 as shown in **Figs. 17b**. The SMA reinforcement ratio exhibited the most significant influence
 474 (32.62% contribution) on the residual drift of hybrid SMA/steel reinforced hollow section piers,
 475 as shown in **Figs. 17b** and **18b**. This observation signifies the efficacy of the SMA reinforcement
 476 in controlling the residual drift. The longitudinal steel reinforcement ratio is the second most
 477 important factor (22.44% contribution) that significantly affects the residual drift (**Figs. 17b** and
 478 **18b**). However, the main effects of f'_c and ρ_{st} on the residual drift are less prominent with less
 479 than 5% contribution, as shown in **Fig. 18b**.

480 The interaction of SMA reinforcement and longitudinal steel reinforcement ratio is the most
 481 prominent interaction effect on the residual drift, as observed in **Figs. 17b** and **18b**. As discussed
 482 earlier, the increase in reinforcement ratio of both the longitudinal steel bars and SMA bars
 483 increases the load capacity of the piers at all damage states; however, the former had an adverse
 484 effect in controlling the residual drift, unlike the SMA reinforcement. An increase in the SMA
 485 reinforcement ratio significantly enhances the load capacity of the piers at the same time
 486 minimizing the residual drift. Thus, it has a desirable effect on both the load capacity and
 487 permanent drift. With the complete replacement of the steel reinforcement bars with SMA in the
 488 plastic hinge region, the residual drift can be minimized while achieving the required load capacity,
 489 however, it is associated with high material costs. Thus, an optimum design is required based on
 490 the allowable residual drift and required load capacity to achieve an economical design. **Figure 19**
 491 shows the contour plot of ρ_{SMA} versus ρ_{sl} to predict the residual drift of the piers. The interaction
 492 between the longitudinal steel reinforcement and SMA reinforcement can also be observed in **Fig.**
 493 **20a**. The variation of the residual drift with the other significant interactions can also be observed
 494 in **Figs. 20b–20e**.

495



496 **Fig. 19:** Contour plot of ρ_{SMA} and ρ_{sl} for predicting the residual drift.



497 **Fig. 20:** Variation of residual drift with (a) ρ_{SMA} and ρ_{st} , (b) f'_c and P/P_0 , (c) H/D and ρ_{st} , (d)
 498 P/P_0 and ρ_{st} , and (e) ρ_{SMA} and H/D .

499

500 **4.2.4. Energy dissipation capacity**

501 The ANOVA results for the energy dissipation at different damage states are summarized in **Table**
 502 **6**. For the slight and moderate damage states, the ANOVA results demonstrate the significance
 503 of the main effects of all parameters on the energy dissipation. However, the effects of f_y and ρ_{st} are
 504 insignificant on the energy dissipation at DS3 and DS4, respectively, as listed in **Table 6**.

505 **Table 6:** ANOVA results for the energy dissipation

Damage states	DS4	DS3	DS2	DS1
Main Parameters				
A f'_c	< 0.0001	< 0.0001	< 0.0001	< 0.0001
B f_y	< 0.0001	0.6254	< 0.0001	< 0.0001
C ρ_{sl}	< 0.0001	< 0.0001	< 0.0001	< 0.0001
D ρ_{st}	0.2621	< 0.0001	0.0014	0.0031
E H/d	< 0.0001	< 0.0001	< 0.0001	< 0.0001
F ρ_{SMA}	< 0.0001	< 0.0001	< 0.0001	< 0.0001
G P/P_0	< 0.0001	< 0.0001	< 0.0001	< 0.0001
Two-way interactions				
AB	0.6138	0.7677	0.8873	0.3585
AC	0.3184	0.0034	0.0085	0.1916
AD	0.0075	0.0412	0.1222	0.5045
AE	0.2608	0.0006	0.0629	0.0133
AF	0.6978	0.0025	0.0116	0.2931
AG	< 0.0001	< 0.0001	0.1653	< 0.0001
BC	0.1467	0.0045	< 0.0001	0.0001
BD	0.3572	0.7657	0.6544	0.3835
BE	< 0.0001	< 0.0001	0.0108	< 0.0001
BF	0.0032	0.0122	0.8136	0.0047
BG	0.9011	0.4793	0.569	0.0036
CD	0.7993	0.348	0.2151	0.6808
CE	< 0.0001	< 0.0001	< 0.0001	< 0.0001
CF	0.0004	< 0.0001	< 0.0001	0.9844
CG	0.0146	0.9623	0.9511	0.8832
DE	0.0604	0.2699	0.0303	0.5453
DF	0.7672	0.5272	0.8172	0.7003
DG	0.333	< 0.0001	< 0.0001	0.0009
EF	< 0.0001	< 0.0001	< 0.0001	0.0006
EG	0.9484	< 0.0001	< 0.0001	0.4916
FG	0.2796	0.0012	< 0.0001	< 0.0001

506
507 The degree and direction of the significant effects on the energy dissipation at various damage
508 states can also be observed in **Figs. 21a–21d**. As shown in these figures, the aspect ratio produces
509 the most prominent negative effect on the energy dissipation at all damage states. Moreover, the
510 longitudinal reinforcement ratio produces the highest positive significant effect on the energy
511 dissipation at all damage states apart from DS1, as shown in **Figs. 21a–21d**.

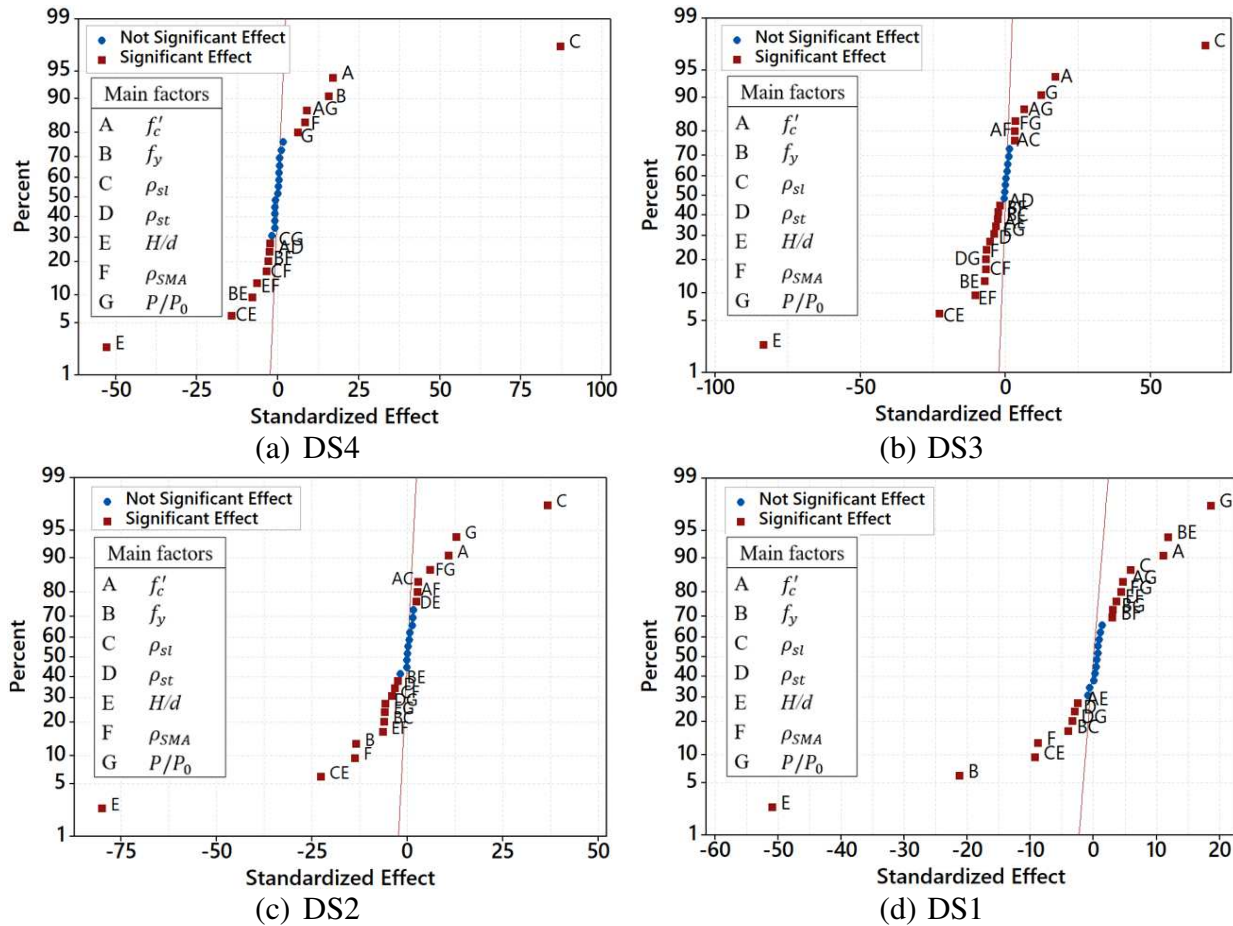
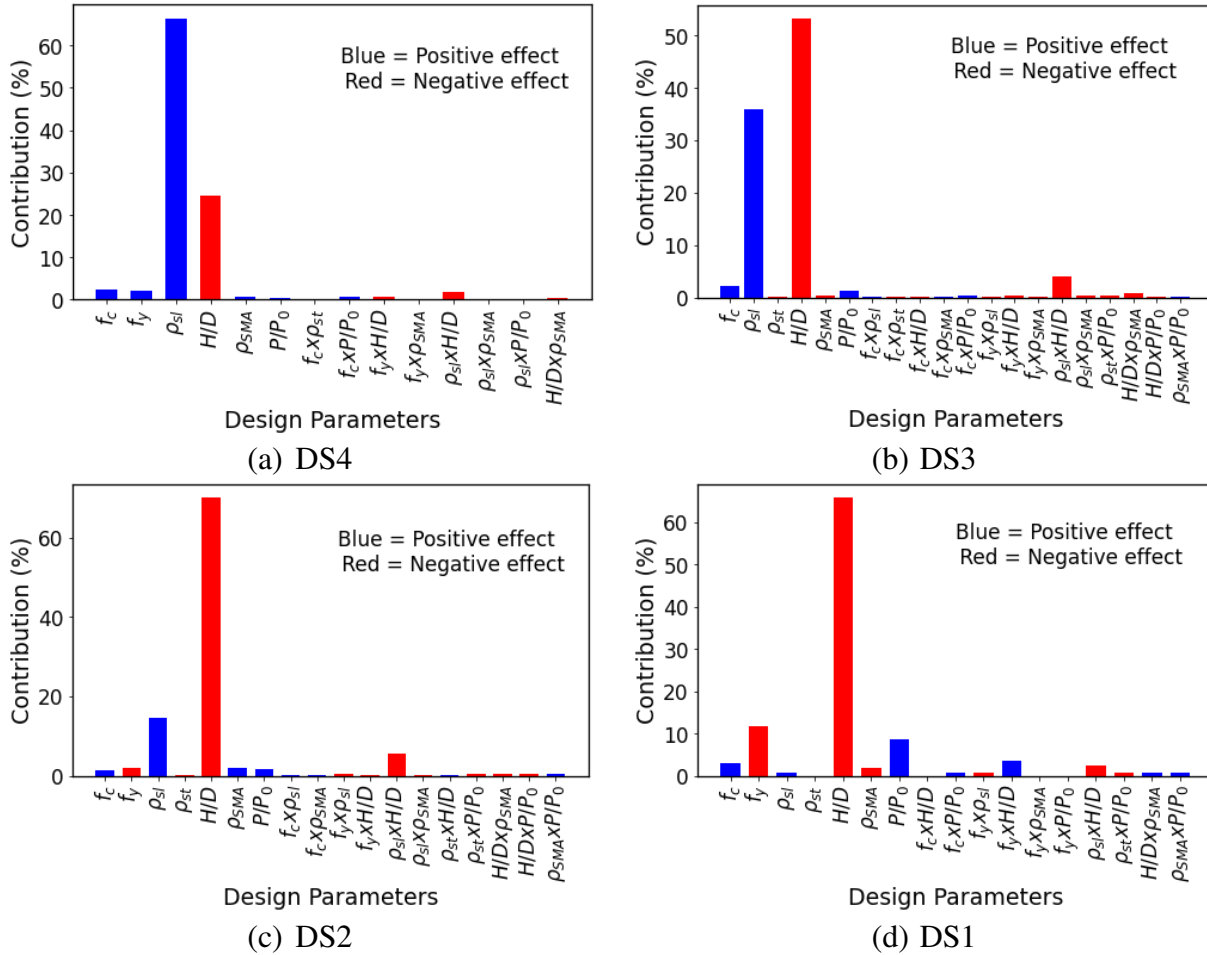


Fig. 21: Normal plot of the standardized effects for energy dissipation.

512
513
514
515
516
517
518
519
520
521
522
523
524
525
526

Figures 22a–22d further clarifies the contributions of the main and interaction effects on the energy dissipation at DS4, DS3, DS2, and DS1, respectively. As can be observed in these figures, the longitudinal steel reinforcement ratio and aspect ratio are the two most prominent factors at DS2, DS3, and DS4 damage states. The effect of longitudinal reinforcement ratio on the energy dissipation increased with the damage states. For instance, at DS1 the contribution of ρ_{st} was only 0.58% which is increased to 14.67%, 36.02%, and 66.29% at DS2, DS3, and DS4, respectively, as shown in **Figs. 22a–22d**. At a slight damage state, the yield strength of steel reinforcement bars showed the highest positive effect (11.63% contribution) on the energy dissipation, as shown in **Figs. 22d** and **22d**. The percentage contribution of the interaction effects varied from 0.03% to 5.65% (**Figs. 22a–22d**). At all limit states except DS1, the $\rho_{st} \times H/d$ interaction showed the highest significant effect on the energy dissipation, as shown in **Figs. 22a–22c**. However, at DS1 the $f_y \times H/d$ interaction was most significant, as shown in **Fig. 22d**.



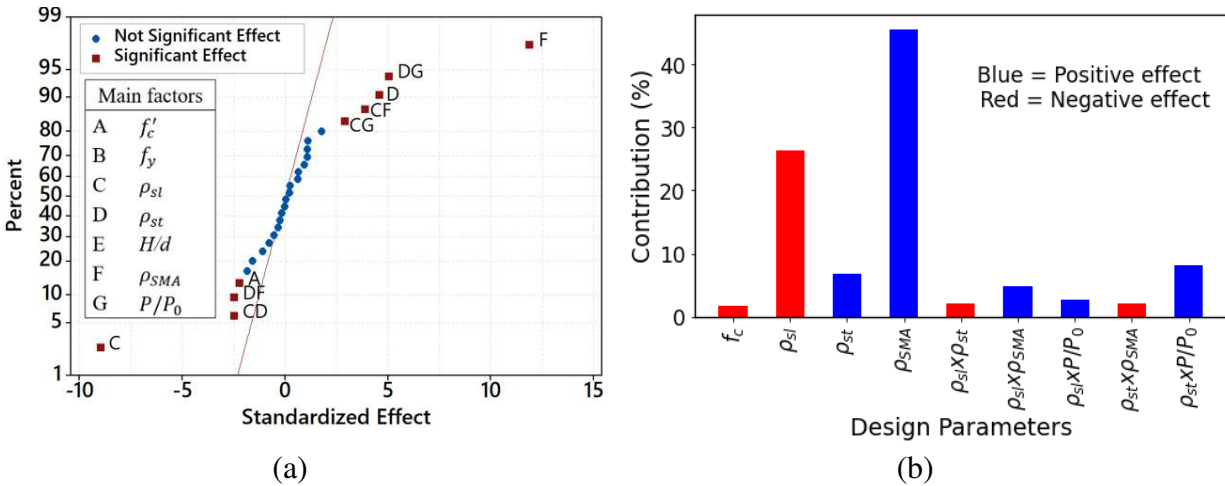
527 **Fig. 22:** Percentage contribution of the significant effects on the energy dissipation.

528

529 **4.2.5. Self-centering efficiency**

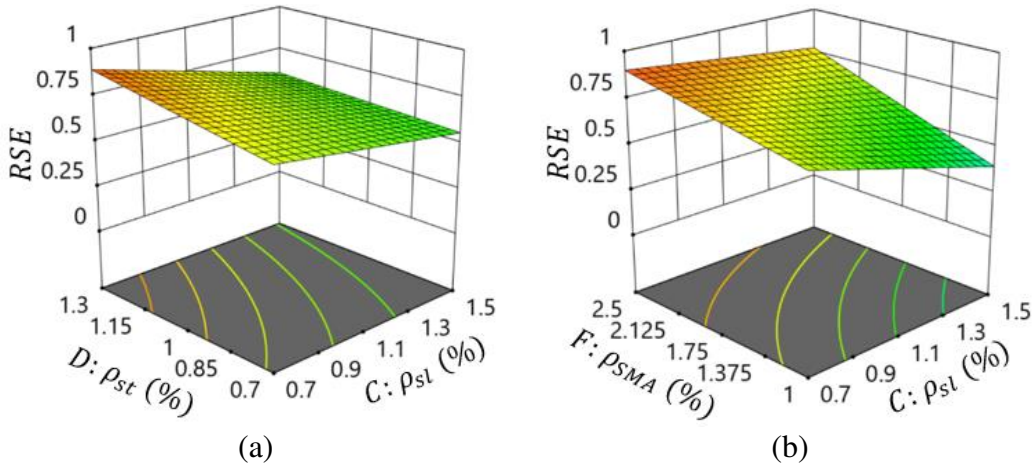
530 The ANOVA results in **Table 5** for relative self-centering efficiency demonstrate the significant
 531 influences of the f'_c , ρ_{sl} , ρ_{st} , and ρ_{SMA} on the self-centering capacity of the novel hollow section
 532 bridge piers. The SMA reinforcement ratio and ρ_{st} exhibited positive standardized effect on the
 533 *RSE*. Consequently, the self-centering capacity increases with the increase in ρ_{SMA} and ρ_{st} .
 534 However, the increase in the ρ_{sl} and f'_c reduce the self-centering capacity of the piers as they have
 535 negative standardized effect on the *RSE* (**Fig. 23a**).

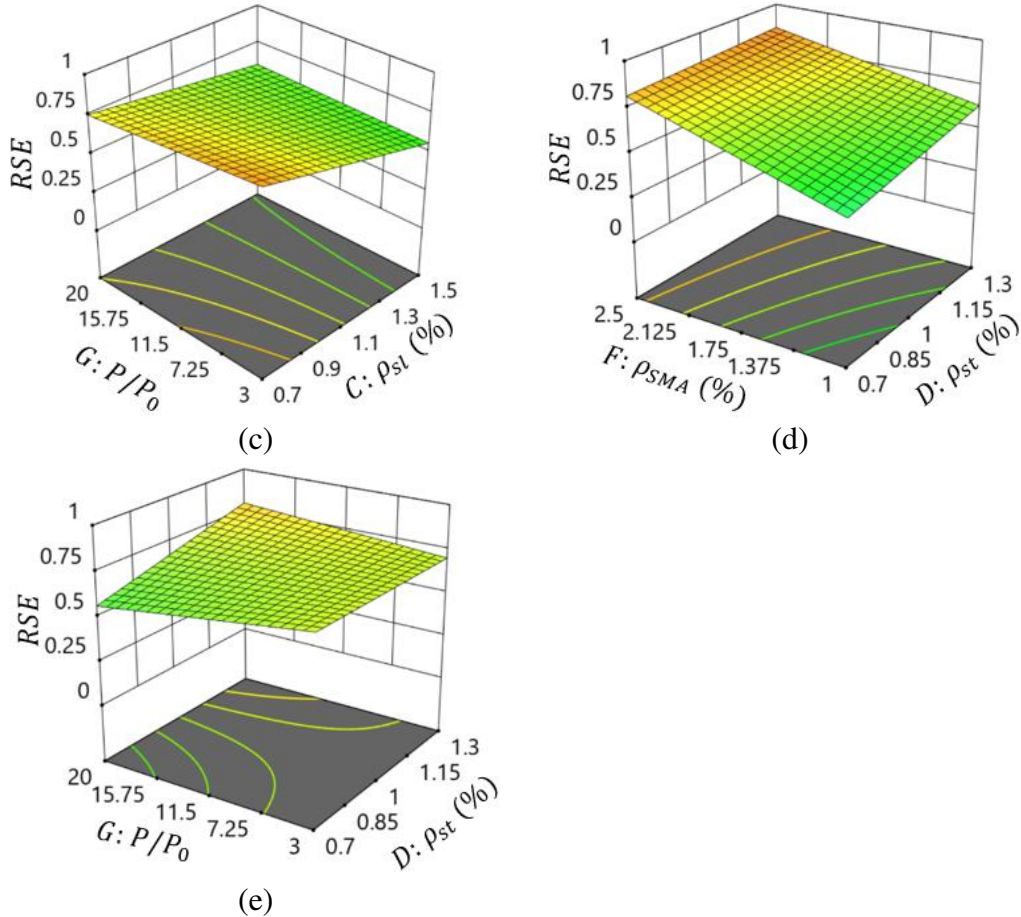
536 The contributions of the significant factors and interactions on the *RSE* are shown in **Fig. 23b**.
 537 The self-centering capacity of the hybrid NSM-SMA/steel reinforced hollow section piers is
 538 mostly influenced by the SMA reinforcement (45.61% contribution) confirming the efficacy of
 539 SMA reinforcement in enhancing the self-centering capacity of the piers, as shown in **Figs. 23a**
 540 and **23b**. The longitudinal steel reinforcement ratio is the second most significant factor with
 541 26.26% contribution on the *RSE*; however, unlike the SMA reinforcement its effect is negative, as
 542 shown in **Figs. 23a** and **23b**. The compressive strength of concrete has the least main significant
 543 influence on the *RSE* (**Figs. 23a** and **23b**).



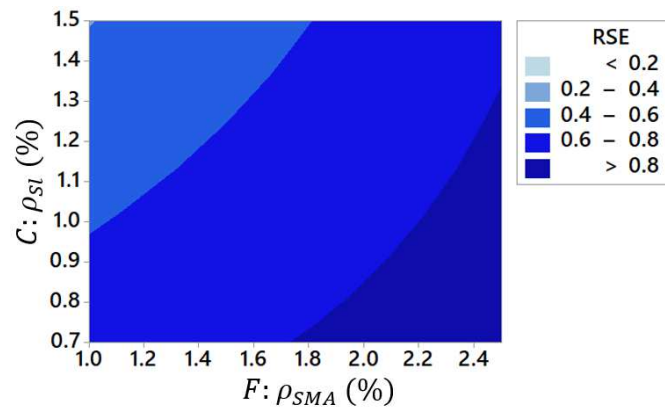
544 **Fig. 23:** Normal plot of the standardized effects (a) and percentage contribution (b) for *RSE*.
 545

546 Regarding the interaction effects, the $\rho_{sl} \times \rho_{st}$, $\rho_{sl} \times P/P_0$, $\rho_{st} \times P/P_0$ interactions significantly
 547 influence the *RSE*, as shown in **Fig. 23a** and **Table 5**. Similarly, the influences of the interactions
 548 of SMA reinforcement ratio with longitudinal steel reinforcement ratio in the plastic hinge zone
 549 and volumetric ratio of transverse reinforcement on the self-centering capacity are significant, as
 550 observed in **Fig. 23a** and **Table 5**. The volumetric ratio of transverse reinforcement and its
 551 interaction with other factors contribute up to 23.79%, as shown in **Fig. 23b**. Among the interaction
 552 effects, the $\rho_{st} \times P/P_0$ and $\rho_{SMA} \times \rho_{sl}$ interactions showed the most significant influence on the
 553 *RSE*, as can be seen in **Figs. 23a** and **23b**. The interaction effects can also be clearly observed in
 554 the 3D plots in **Figs. 24a–24d**. Moreover, **Fig. 25** shows the contour plot of ρ_{SMA} versus ρ_l for
 555 predicting the *RSE*.
 556





557 **Fig. 24:** Variation of residual drift with (a) ρ_{sl} and ρ_{st} , (b) ρ_{SMA} and ρ_{sl} , (c) P/P_0 and ρ_{sl} , (d)
 558 ρ_{SMA} and ρ_{st} , and (e) P/P_0 and ρ_{st} .
 559



560 **Fig. 25:** Contour plot of ρ_{SMA} and ρ_{sl} for predicting the RSE.
 561

562 4.3. Regression equation for the responses

563 A regression equation is obtained in this section to better understand the effects of the key design
 564 factors and significant interactions on the cyclic performance of hybrid SMA/steel reinforced
 565 hollow section bridge piers. The results of sensitivity analysis in factorial DOE can be used to
 566 obtain the relationship between the input factors and the response variables. Thus, the response of

567 hybrid SMA/steel reinforced hollow bridge piers for different levels of each factor can be estimated
 568 the following general equation.

$$\begin{aligned}
 R = & a_0 + a_1A + a_2B + a_3C + a_4D + a_5E + a_6F + a_7G + a_8AD + a_9AE + a_{10}AG \\
 & + a_{11}BE + a_{12}CD + a_{13}CE + a_{14}CF + a_{15}CG + a_{16}DE + a_{17}DF \\
 & + a_{18}DG + a_{19}EF + a_{20}EG + a_{21}FG
 \end{aligned} \quad (7)$$

569 where R is the response variable for different levels of each factor, a_0 is the intercept, and a_1
 570 through a_{21} are the regression coefficients for each significant factor and interaction.

571 The values of the regression coefficients and the intercept for each response variable are given
 572 in **Table 7** based on the results of sensitivity analysis. The response variables include the initial
 573 stiffness, residual drift, relative self-centering efficiency, and lateral load capacity at different limit
 574 states, as listed in **Table 7**. The regression equation in Eq. (7) can be used for preliminary design;
 575 however, a detailed design procedure is required for the application of the novel bridge piers. Thus,
 576 in future research, a detailed design guideline for the novel hybrid SMA/steel reinforced hollow
 577 section piers considering the significant factors and interactions will be proposed. The applicability
 578 of Eq. (7) is limited to the following ranges of the input parameters: $27 \text{ MPa} \leq f'_c \leq 48 \text{ MPa}$;
 579 $420 \text{ MPa} \leq f_y \leq 550 \text{ MPa}$; $0.70\% \leq \rho_{sl} \leq 1.50\%$; $0.70 \leq \rho_{st} \leq 1.30$; $4 \leq H/d \leq 7$; $1\% \leq$
 580 $\rho_{SMA} \leq 2.5\%$; and $3\% \leq P/P_0 \leq 20\%$, as listed in **Table 3**.

581 **Table 7:** ANOVA results for the energy dissipation

Coefficient	Factor	Initial stiffness	Residual drift	RSE	P_{max}			
					DS1	DS2	DS3	DS4
a_0	-	18.57	1.7000	0.6934	1063.08	1359.98	1400.01	1429.22
a_1	A: f'_c	1.820	0.2428	-0.0273	105.52	102.73	100.31	90.60
a_2	B: f_y	0.607	0.0000	0.0000	31.92	65.55	67.98	71.49
a_3	C: ρ_{sl}	1.760	0.6376	-0.1090	102.47	142.07	148.16	152.89
a_4	D: ρ_{st}	0.000	-0.3006	0.0551	0.00	0.00	0.00	0.00
a_5	E: H/d	-11.27	0.5658	0.0000	-425.46	-463.59	-461.13	-474.38
a_6	F: ρ_{SMA}	1.370	-0.7688	0.1437	77.46	188.82	210.62	221.09
a_7	G: P/P_0	3.640	0.0000	0.0000	211.35	198.06	170.76	141.54
a_8	AD	0.000	0.0000	0.0000	0.00	-22.88	-26.49	-28.38
a_9	AE	-1.040	0.0000	0.0000	-37.13	-37.25	-37.28	-35.14
a_{10}	AG	1.350	0.2501	0.0000	77.51	95.03	93.65	103.36
a_{11}	BE	-0.516	0.0000	0.0000	-24.34	-27.36	-24.80	-25.51
a_{12}	CD	0.000	0.0000	-0.0304	0.00	0.00	0.00	0.00
a_{13}	CE	-1.210	0.0000	0.0000	-52.43	-44.95	-41.62	-43.56
a_{14}	CF	0.000	-0.3234	0.0466	0.00	0.00	0.00	0.00
a_{15}	CG	0.000	0.0000	0.0350	0.00	0.00	0.00	0.00
a_{16}	DE	0.000	-0.2280	0.0000	0.00	0.00	0.00	0.00
a_{17}	DF	0.000	0.0000	-0.0304	0.00	0.00	0.00	0.00
a_{18}	DG	0.000	-0.2970	0.0608	0.00	31.31	33.45	30.83
a_{19}	EF	-1.010	-0.1934	0.0000	-44.44	-68.72	-61.08	-63.88
a_{20}	EG	-2.180	0.0000	0.0000	-81.82	-71.46	-66.20	-52.96
a_{21}	FG	0.000	0.0000	0.0000	0.00	0.00	-31.12	-41.60

583 5. Conclusions

584 This paper presented a numerical investigation on the seismic response of novel hollow section
585 bridge piers reinforced with hybrid superelastic shape memory alloy (SMA) and steel bars under
586 reverse cyclic and constant axial loading. The performance of the piers in terms of hysteretic
587 characteristics, energy dissipation capacity, permanent (residual) deformation, and self-centering
588 capacity was numerically investigated and compared with the conventional reinforced concrete
589 (RC) pier. The performance of the novel hybrid SMA/steel reinforced hollow bridge piers was first
590 investigated using four types of commercially available superelastic SMA bars and compared with
591 the conventional RC pier of the same flexural capacity. The hybrid SMA/steel reinforced piers
592 developed significantly improved seismic responses in terms of the residual drift and self-centering
593 capacity. The sensitivity analysis was used to explore the effect of various key design factors and
594 their interactions on the performance of the hybrid SMA/steel reinforced piers at different damage
595 states. The following conclusions can be drawn from the results of the current study:

- 596 • The hybrid SMA/steel reinforcement was effective in controlling the residual drift and thus
597 enhance the resilience of hollow bridge piers.
- 598 • The hybrid SMA/steel reinforced piers showed a significantly higher self-centering
599 capacity compared to the reference pier.
- 600 • The most significant design parameters associated with the initial stiffness are the axial
601 load ratio and aspect ratio of the piers. The initial stiffness increases with an increase in f'_c ,
602 f_y , ρ_{sl} , ρ_{SMA} , and P/P_0 , while it decreases with H/D and its interaction with f'_c , f_y , ρ_{sl} ,
603 ρ_{SMA} , and P/P_0 .
- 604 • The SMA reinforcement ratio produced the most prominent positive effect on the lateral
605 load capacity at DS4 and DS3. However, its effect is reduced for the other two damage
606 states. Particularly, for the slight damage state, the contribution of ρ_{SMA} is less than 5%.
- 607 • The reinforcement ratio of SMA in the plastic hinge zone has the highest significant
608 influence on the residual drift followed by ρ_{sl} . Similarly, the interaction between the
609 reinforcement ratio of steel bars and SMA was the most significant interaction effect on
610 the residual drift. The increase in the ρ_{SMA} limits the residual drift, thus, it is effective in
611 controlling the residual drift and enhance the seismic resilience of the piers. However, the
612 longitudinal reinforcement had an adverse effect on the residual drift behavior as it
613 increases the permanent drift.
- 614 • The self-centering capacity of the novel bridge piers was mainly influenced by the SMA
615 reinforcement ratio. Among the interaction effects, the $\rho_{SMA} \times \rho_l$ interaction showed the
616 most prominent influence on the self-centering capacity.
- 617 • Finally, a regression equation based on the results of factorial DOE is proposed to predict
618 the responses of the novel hollow section pier at different levels of the main factors.

619 The seismic performance of the hybrid SMA/steel reinforced hollow bridge piers is
620 investigated in this study for the first time. Moreover, the current study identified the most
621 prominent design parameters on the performance of the novel hollow bridge piers. The results
622 presented in this study are beneficial for future research on the design of hybrid SMA/steel
623 reinforced hollow bridge piers. Future study is recommended to accurately define the damage
624 states and develop detailed performance-based seismic design guidelines for the hybrid SMA/steel
625 reinforced piers based on a series of experimental and analytical investigations.

626

627 **Declarations**

628 **Funding** This research is funded by Natural Sciences and Engineering Research Council of
629 Canada through Discovery Grant 2020.

630 **Conflict of interest** The authors declare that they have no conflict of interest.

631 **Acknowledgment**

632 The financial contribution of Natural Sciences and Engineering Research Council of Canada
633 through Discovery Grant was critical to conduct this research and is gratefully acknowledged.

634

635 **References**

- 636 Abdulridha A, Palermo D, Foo S, Vecchio FJ (2013) Behavior and modeling of superelastic shape
637 memory alloy reinforced concrete beams. *Eng Struct* 49:893–904.
638 <https://doi.org/10.1016/j.engstruct.2012.12.041>
- 639 Abraik E, Youssef MA (2021) Ductility and overstrength of shape-memory-alloy reinforced-concrete
640 shear walls. *Eng Struct* 239:. <https://doi.org/10.1016/j.engstruct.2021.112236>
- 641 ACI Committee 318 (2011) Building Code Requirements for Structural Concrete and commentary (ACI
642 318–14). Am Concr Institute, Farmingt Hills, MI 524
- 643 Akbari R (2012) Seismic fragility analysis of reinforced concrete continuous span bridges with irregular
644 configuration. *Struct Infrastruct Eng* 8:873–889. <https://doi.org/10.1080/15732471003653017>
- 645 AlAjarmeh OS, Manalo AC, Benmokrane B, et al (2020) Hollow concrete columns: Review of structural
646 behavior and new designs using GFRP reinforcement. *Eng Struct* 203:109829.
647 <https://doi.org/10.1016/j.engstruct.2019.109829>
- 648 Alam MS, Youssef MA, Nehdi M (2008) Analytical prediction of the seismic behaviour of superelastic
649 shape memory alloy reinforced concrete elements. *Eng Struct* 30:3399–3411.
650 <https://doi.org/10.1016/j.engstruct.2008.05.025>
- 651 Auricchio F, Sacco E (1997) A Superelastic Shape-memory-alloy Beam Model. *J Intell Mater Syst*
652 8:489–501
- 653 Berry MP, Eberhard MO (2005) Practical performance model for bar buckling. *J Struct Eng* 131:1060–
654 1070. [https://doi.org/10.1061/\(ASCE\)0733-9445\(2005\)131](https://doi.org/10.1061/(ASCE)0733-9445(2005)131)
- 655 Berry MP, Eberhard MO (2007) Performance Modeling Strategies for Modern Reinforced Concrete
656 Bridge Columns PEER Report 2007/07 Pacific Earthquake Engineering Research Center, College of
657 Engineering, University of California, Berkeley, USA
- 658 Billah AHMM, Alam MS (2012) Seismic performance of concrete columns reinforced with hybrid shape
659 memory alloy (SMA) and fiber reinforced polymer (FRP) bars. *Constr Build Mater* 28:730–742.
660 <https://doi.org/10.1016/j.conbuildmat.2011.10.020>
- 661 Billah AHMM, Alam MS (2016) Performance-Based Seismic Design of Shape Memory Alloy–
662 Reinforced Concrete Bridge Piers. I : Development of Performance-Based Damage States. *J Struct*
663 *Eng* 142:04016140. [https://doi.org/10.1061/\(ASCE\)ST.1943-541X.0001458](https://doi.org/10.1061/(ASCE)ST.1943-541X.0001458)
- 664 Billah AHMM, Shahria Alam M (2016) Plastic hinge length of shape memory alloy (SMA) reinforced
665 concrete bridge pier. *Eng Struct* 117:321–331. <https://doi.org/10.1016/j.engstruct.2016.02.050>
- 666 Canadian Standards Association (2019) CAN/CSA S6-19 (2019) Canadian Highway Bridge Design
667 Code. CAN/CSA S6-19
- 668 Christopoulos C, Tremblay R, Kim H-J, Lacerte M (2008) Self-Centering Energy Dissipative Bracing
669 System for the Seismic Resistance of Structures: Development and Validation. *J Struct Eng* 134:96–
670 107. [https://doi.org/10.1061/\(ASCE\)0733-9445\(2008\)134](https://doi.org/10.1061/(ASCE)0733-9445(2008)134)
- 671 Dahal PK, Tazarv M (2020) Mechanical bar splices for incorporation in plastic hinge regions of RC
672 members. *Constr Build Mater* 258:. <https://doi.org/10.1016/j.conbuildmat.2020.120308>

673 DesRoches R, McCormick J, Delemont M (2004) Cyclic Properties of Superelastic Shape Memory Alloy
674 Wires and Bars. *J Struct Eng* 130:38–46. [https://doi.org/10.1061/\(ASCE\)0733-9445\(2004\)130](https://doi.org/10.1061/(ASCE)0733-9445(2004)130)
675 FEMA (2003) Multi-hazard Loss Estimation Methodology: Earthquake Model, HAZUS-MH 2.1:
676 Technical Manual. . Federal Emergency Management Agency, Washington, DC
677 Feng Y, Kowalsky M, Nau JM (2015) Effect of Seismic Load History on Deformation Limit States for
678 Longitudinal Bar Buckling in RC Circular Columns. *J Struct Eng* 141:1–13.
679 [https://doi.org/10.1061/\(ASCE\)ST.1943-541X.0001153](https://doi.org/10.1061/(ASCE)ST.1943-541X.0001153)
680 Filippou FC, Popov EP, Bertero V V. (1983) Effects of Bond Deterioration on Hysteretic Behavior of
681 Reinforced Concrete Joints. Report EERC 83-19, Earthquake Engineering Research Center,
682 University of California, Berkeley.
683 Fujino Y, Hashimoto S, Abe M (2005) Damage Analysis of Hanshin Expressway Viaducts during 1995
684 Kobe Earthquake. I: Residual Inclination of Reinforced Concrete Piers. *J Bridg Eng* 10:45–53.
685 [https://doi.org/10.1061/\(ASCE\)1084-0702\(2005\)10](https://doi.org/10.1061/(ASCE)1084-0702(2005)10)
686 Ghassemieh M, Mostafazadeh M, Sadeh MS (2012) Seismic control of concrete shear wall using shape
687 memory alloys. *J Intell Mater Syst Struct* 23:535–543. <https://doi.org/10.1177/1045389X12436731>
688 Goodnight JC, Kowalsky M, Nau JM (2016) Strain Limit States for Circular RC Bridge Columns. *Earthq*
689 *Spectra* 32:1627–1652. <https://doi.org/10.1193/030315EQS036M>
690 Hosseini F, Gencturk B (2019) Structural assessment of bridge columns with engineered cementitious
691 composites and Cu-Al-Mn superelastic alloys. *Constr Build Mater* 203:331–342.
692 <https://doi.org/10.1016/j.conbuildmat.2019.01.102>
693 Hosseini F, Gencturk B, Jain A, Shahzada K (2019) Optimal design of bridge columns constructed with
694 engineered cementitious composites and Cu-Al-Mn superelastic alloys. *Eng Struct* 198:.
695 <https://doi.org/10.1016/j.engstruct.2019.109531>
696 Hosseini F, Gencturk B, Lahpour S, Gil DI (2015) An experimental investigation of innovative bridge
697 columns with engineered cementitious composites and Cu-Al-Mn super-elastic alloys. *Smart Mater*
698 *Struct* 24:.
699 <https://doi.org/10.1088/0964-1726/24/8/085029>
700 Kent DC, Park R (1971) Flexural members with confined concrete. *J Struct Div* 97 (ST7):1969–1990
701 Kim SH, Shinozuka M (2004) Development of fragility curves of bridges retrofitted by column jacketing.
702 *Probabilistic Eng Mech* 19:105–112. <https://doi.org/10.1016/j.probenmech.2003.11.009>
703 Kusumawardaningsih Y, Hadi MNS (2010) Comparative behaviour of hollow columns confined with
704 FRP composites. *Compos Struct* 93:198–205. <https://doi.org/10.1016/j.compstruct.2010.05.020>
705 Liang X, Sritharan S (2018) Effects of Confinement in Circular Hollow Concrete Columns. *J Struct Eng*
706 144:04018159. [https://doi.org/10.1061/\(ASCE\)ST.1943-541X.0002151](https://doi.org/10.1061/(ASCE)ST.1943-541X.0002151)
707 Mander JB, Priestley MJN, Park R (1989) Theoretical Stress-Strain Model for Confined Concrete. *J*
708 *Struct Eng* 114:1804–1826
709 Mao J, Jia D, Yang Z, Xiang N (2019) Seismic Performance of Concrete Bridge Piers Reinforced with
710 Hybrid Shape Memory Alloy (SMA) and Steel Bars. *J Earthq Tsunami* 14:.
711 <https://doi.org/10.1142/S1793431120500013>
712 McKenna F, Fenves GL, Scott MH (2000) Open System for Earthquake Engineering Simulation.
713 PACIFIC Earthq Eng Res Cent
714 Menegotto M, Pinto. PE (1973) Method of analysis for cyclically loaded R .C. plane frames including
715 changes in geometry and non-elastic behaviour of elements under combined normal force and
716 bending IABSE Symposium on the Resistance and Ultimate Deformability of Structures. Lisbon,
717 Portugal
718 Montgomery DC (2013) Design and Analysis of Experiments, 8th edn. John Wiley & Sons Inc, Hoboken,
719 New Jersey, USA
720 Mostafa Tazarv M. Saiid Saiidi (2015) Design and Construction of Bridge Columns Incorporating
721 Mechanical Bar Spllices in Plastic Hinge Zones
722 Nahar M, Billah AHMM, Kamal HR, Islam K (2019) Numerical seismic performance evaluation of
723 concrete beam-column joint reinforced with different super elastic shape memory alloy rebars. *Eng*
Struct 194:161–172. <https://doi.org/10.1016/j.engstruct.2019.05.054>

724 Navarro-Gómez A, Bonet JL (2019) Improving the seismic behaviour of reinforced concrete moment
725 resisting frames by means of SMA bars and ultra-high performance concrete. *Eng Struct* 197:.
726 <https://doi.org/10.1016/j.engstruct.2019.109409>

727 Noguez CAC, Saiidi MS (2012) Shake-Table Studies of a Four-Span Bridge Model with Advanced
728 Materials. *J Struct Eng* 138:183–192. [https://doi.org/10.1061/\(ASCE\)ST.1943-541X.0000457](https://doi.org/10.1061/(ASCE)ST.1943-541X.0000457)

729 Omori T, Ando K, Okano M, et al (2011) Superelastic Effect in Polycrystalline Ferrous Alloys. *Science*
730 (80-) 333:68–71

731 Palermo D, Abdulridha A, Leonardo W, Puentes C (2006) Performance of Superelastic Shape Memory
732 Alloy Reinforced Concrete Members. In: *SMAR 2015-3rd Conf. on Smart Monitoring, Assessment*
733 *and Rehabilitation of Civil Structures*. pp 1–8

734 Parghi A, Alam MS (2017) Seismic collapse assessment of non-seismically designed circular RC bridge
735 piers retrofitted with FRP composites. *Compos Struct* 160:901–916.
736 <https://doi.org/10.1016/j.compstruct.2016.10.094>

737 Parghi A, Alam MS (2016) Seismic behavior of deficient reinforced concrete bridge piers confined with
738 FRP – A fractional factorial analysis. *Eng Struct* 126:531–546.
739 <https://doi.org/10.1016/j.engstruct.2016.08.011>

740 Paulay T, Priestley MJN (1992) *Seismic design of reinforced concrete and masonry buildings*

741 Pereiro-Barceló J, Bonet JL, Cabañero-Escudero B, Martínez-Jaén B (2019) Cyclic behavior of hybrid
742 RC columns using High-Performance Fiber-Reinforced Concrete and Ni-Ti SMA bars in critical
743 regions. *Compos Struct* 212:207–219. <https://doi.org/10.1016/j.compstruct.2019.01.029>

744 Priestley MJN, Seible F, Calvi G (1996) *Seismic Design and Retrofit of Bridges*. Wiley, New York

745 Ramirez CM, Miranda E (2012) Significance of residual drifts in building earthquake loss estimation.
746 *Earthq Eng Struct Dyn* 41:1477–1493. <https://doi.org/10.1002/eqe>

747 Ranzo G, Priestley MJN (2001) Seismic performance of circular hollow columns subjected to high shear.
748 *Struct Syst Res Proj*

749 Reza SM, Alam MS, Tesfamariam S (2014) Lateral load resistance of bridge piers under flexure and
750 shear using factorial analysis. *Eng Struct* 59:821–835.
751 <https://doi.org/10.1016/j.engstruct.2013.12.009>

752 Saiidi MS, O'Brien M, Sadrossadat-zadeh M (2009) Cyclic Response of Concrete Bridge Columns Using
753 Superelastic Nitinol and Bendable Concrete. *ACI Struct J* 106:69–77

754 Saiidi MS, Wang H (2006) Exploratory Study of Seismic Response of Concrete Columns with Shape
755 Memory Alloys Reinforcement. *ACI Struct J* 103:436–443

756 Shrestha K, Araki Y, Nagae T, et al (2013) Feasibility of Cu – Al – Mn superelastic alloy bars as
757 reinforcement elements in concrete beams. *Smart Mater Struct* 22:025025.
758 <https://doi.org/10.1088/0964-1726/22/2/025025>

759 Sideris P, Aref AJ, Filiatrault A (2014) Quasi-Static Cyclic Testing of a Large-Scale Hybrid Sliding-
760 Rocking Segmental Column with Slip-Dominant Joints. *J Bridg Eng* 19:04014036.
761 [https://doi.org/10.1061/\(asce\)be.1943-5592.0000605](https://doi.org/10.1061/(asce)be.1943-5592.0000605)

762 Taucer FF, Spacone E, Filippou FC (1991) *A Fiber Beam-Column Element for Seismic Response*
763 *Analysis of Reinforced Concrete Structures*, Report No. UCB/EERC-91/17: Earthquake Engineering
764 Research Center College of Engineering University of California, Berkeley

765 Tazarv M, Saiidi MS (2016a) Seismic design of bridge columns incorporating mechanical bar splices in
766 plastic hinge regions. *Eng Struct* 124:507–520. <https://doi.org/10.1016/j.engstruct.2016.06.041>

767 Tazarv M, Saiidi MS (2016b) Low-Damage Precast Columns for Accelerated Bridge Construction in
768 High Seismic Zones. *J Bridg Eng* 21:04015056. [https://doi.org/10.1061/\(ASCE\)BE.1943-5592.0000806](https://doi.org/10.1061/(ASCE)BE.1943-5592.0000806)

769

770 Tazarv M, Saiidi MS (2015) Reinforcing NiTi Superelastic SMA for Concrete Structures. *J Struct Eng*
771 141:04014197. [https://doi.org/10.1061/\(ASCE\)ST.1943-541X.0001176](https://doi.org/10.1061/(ASCE)ST.1943-541X.0001176)

772 Wang B, Zhu S (2018) Seismic behavior of self-centering reinforced concrete wall enabled by
773 superelastic shape memory alloy bars. *Bull Earthq Eng* 16:479–502. <https://doi.org/10.1007/s10518-017-0213-8>

774

775 Wang Z, Padgett JE, Dueñas-Osorio L (2014) Toward a uniform seismic risk design of reinforced
 776 concrete bridges: A displacement-based approach. *Struct Saf* 50:103–112.
 777 <https://doi.org/10.1016/j.strusafe.2014.03.009>
 778 Wood A, Noy I, Parker M (2016) The Canterbury rebuild five years on from the Christchurch earthquake.
 779 *Reserv Bank New Zeal Bull* 79:1–16
 780 Xiang N, Chen X, Alam MS (2020) Probabilistic seismic fragility and loss analysis of concrete bridge
 781 piers with superelastic shape memory alloy-steel coupled reinforcing bars. *Eng Struct* 207:110229.
 782 <https://doi.org/10.1016/j.engstruct.2020.110229>
 783 Xing G, Ozbulut OE, Al-Dhabyani MA, et al (2020) Enhancing flexural capacity of RC columns through
 784 near surface mounted SMA and CFRP bars. *J Compos Mater* 54:4661–4676.
 785 <https://doi.org/10.1177/0021998320937054>
 786 Yassin MHM (1994) Nonlinear analysis of prestressed concrete structures under monotonic and cycling
 787 loads. PhD dissertation, University of California, Berkeley
 788 Yi JH, Kim SH, Koshiyama S (2007) PDF interpolation technique for seismic fragility analysis of
 789 bridges. *Eng Struct* 29:1312–1322. <https://doi.org/10.1016/j.engstruct.2006.08.019>
 790 Youssef MA, Alam MS, Nehdi M (2008) Experimental Investigation on the Seismic Behavior of Beam-
 791 Column Joints Reinforced with Superelastic Shape Memory Alloys. *J Earthq Eng* 12:1205–1222.
 792 <https://doi.org/10.1080/13632460802003082>
 793 Zheng Y, Dong Y (2019) Performance-based assessment of bridges with steel-SMA reinforced piers in a
 794 life-cycle context by numerical approach. *Bull Earthq Eng* 17:1667–1688.
 795 <https://doi.org/10.1007/s10518-018-0510-x>
 796 Zhu L, Elwood KJ, Haukaas T (2007) Classification and seismic safety evaluation of existing reinforced
 797 concrete columns. *J Struct Eng* 133:1316–1330. [https://doi.org/10.1061/\(ASCE\)0733-9445\(2007\)133:9\(1316\)](https://doi.org/10.1061/(ASCE)0733-9445(2007)133:9(1316))
 799 (2013a) ACI Committee 374, Guide for Testing Reinforced Concrete Structural Elements Under Slowly
 800 Applied Simulated Seismic Loads (ACI 374.2R-13), Farmington Hills, MI, USA,
 801 (2013b) ASCE. Seismic evaluation and retrofit of existing buildings. ASCE/SEI 41-13. Reston, VA:
 802 American Society of Civil Engineers,
 803